Real-time, directional measurement of 8B solar neutrinos in the Kamiokande II detector

doi: 10.1103/PhysRevD.44.2241

Real-time, directional measurement of ^{8}B solar neutrinos in the Kamiokande II detector

K. S. Hirata, K. Inoue, T. Ishida, T. Kajita, K. Kihara, M. Nakahata,
K. Nakamura, S. Ohara,* N. Sato,† Y. Suzuki, Y. Totsuka, and Y. Yaginuma‡
Institute for Cosmic Ray Research, University of Tokyo, Tanashi, Tokyo 188, Japan

M. Mori, Y. Oyama, A. Suzuki, K. Takahashi, and M. Yamada
National Laboratory for High Energy Physics (KEK), Tsukuba, Ibaraki 305, Japan

M. Koshiba and K. Nishijima
Tokai University, Shibuya, Tokyo 151, Japan

T. Suda and T. Tajima§
Department of Physics, Kobe University, Kobe, Hyogo 657, Japan

K. Miyano, H. Miyata, and H. Takei
Niigata University, Niigata, Niigata 950-21, Japan

Y. Fukuda, E. Kodera, Y. Nagashima, and M. Takita
Department of Physics, Osaka University, Toyonaka, Osaka 560, Japan

K. Kaneyuki and T. Tanimori
Department of Physics, Tokyo Institute of Technology, Meguro, Tokyo 152, Japan

E. W. Beier, L. R. Feldscher, E. D. Frank, W. Frati, S. B. Kim,** A. K. Mann,
F. M. Newcomer, R. Van Berg, and W. Zhang††
Department of Physics, University of Pennsylvania, Philadelphia, Pennsylvania 19104
(Received 21 June 1991)

The method of ^{8}B solar-neutrino measurement by means of the reaction $\nu_e e \rightarrow \nu_e e$ in the Kamiokande II detector is described in detail. A data sample of 1040 live detector days in the time period January 1987 through April 1990 yields a clear directional correlation of the solar-neutrino-induced electron events with respect to the Sun and a measurement of the differential electron energy distribution. The measured flux of ^{8}B solar neutrinos from the subsamples of 450 days at electron energy threshold $E_e \geq 9.3$ MeV, and 590 days at $E_e \geq 7.5$ MeV relative to calculations of the ^{8}B flux based on the standard solar model are $0.46 \pm 0.05(\text{stat}) \pm 0.06(\text{syst})$ times the prediction of Bahcall and Ulrich, and $0.70 \pm 0.08(\text{stat}) \pm 0.09(\text{syst})$ times the prediction of Turck-Chièze *et al.* The shape of the recoil electron energy distribution is consistent with that expected from the product of the known shape of the neutrino flux from ^{8}B β decay and the cross section for $\nu_e e \rightarrow \nu_e e$ scattering. Within the statistical error, there is no evidence in the solar-neutrino signal for a significant time variation.

I. INTRODUCTION

The Sun is an intense source of low-energy ($E_e \leq 15$ MeV) electron neutrinos (ν_e) that are products of the nuclear processes in its higher temperature central region which provide the solar energy [1]. Solar neutrinos probe the interior of the Sun, unlike the photons emitted from its surface layer, and thereby provide a sensitive test of solar models. But, also, of special importance to elementary-particle physics, they provide a means of searching for as yet undetected intrinsic properties of neutrinos through the wide range of matter density [2], the very long distance from the Sun to the Earth [3], and the relatively high solar magnetic field traversed by low-energy neutrinos in their passage from the core of the Sun to a detector on Earth [4].

A. The standard solar model

Our knowledge of the Sun, which is formulated in a quantitative description known as the standard solar model (SSM), is based on laboratory measurements and on theoretical models of the internal structure of the Sun. The SSM makes the following assumptions concerning stellar evolution: (1) the interior of the Sun is in hydrostatic equilibrium maintained by a balance of the gravitational force against the radiative and particle pressures; (2) the source of energy in the Sun is nuclear fusion; (3) the energy transport in the Sun is by photons or convective currents; (4) the nuclear abundances change solely by nuclear reactions. The coupled differential equations expressing these assumptions are subjected to constraints of the present measured luminosity, radius, and mass of the

Sun, and its approximate age. Important additional empirical or semiempirical information such as the equation of state, nuclear cross sections at relatively low energies, and the radiative absorption coefficients (opacities) need also to be specified quantitatively. The system of equations and constraints is solved iteratively until agreement with an accuracy of one part in 10^5 is achieved between the model and the observations of the solar luminosity and solar radius. The solution of the SSM yields the primordial values for the mass fraction of hydrogen, helium, and heavy elements, the present physical profiles inside the Sun (e.g., mass, temperature, density, pressure, and luminosity as a function of radius), the spectrum of helioseismic oscillation frequencies at the solar surface, as well as the fluxes and spectra of solar neutrinos [5].

The solar core is believed to be in the hydrogen-burning phase, a sequence of nuclear reactions which converts four hydrogen nuclei into a helium nucleus, two positrons and two neutrinos with a release of 26.7 MeV of which 3% is carried by neutrinos. The SSM predicts that 98.5% of the total solar energy is generated by a series of reactions initiated by the reaction $pp \rightarrow de^+\nu_e$, and the other 1.5% is by the CNO cycle. The total neutrino flux at Earth is $(6.6\times10^{10}/\text{cm}^2)/$ sec, mostly (90%) due to neutrinos from the *pp* reaction, for which the calculated flux is almost independent of the input parameters with an uncertainty of less that 2%. Neutrinos from the $^8\text{B}\rightarrow{}^8\text{Be}^*+e^++\nu_e$ reaction are of particular interest by virtue of their relatively high energies, up to 15 MeV, although the neutrino flux is less than 10^{-4} of the total solar-neutrino flux. The calculated flux of ^{8}B solar neutrinos is uncertain by 30–40 % largely because it depends on the uncertainty in the reaction rate of $^7\text{Be}+p\rightarrow{}^8\text{B}+\gamma$, which is extremely sensitive to the central temperature of the Sun ($\sim T_6^{17}$, where $T_6=T_{\text{core}}/10^6$ K), and to the value of the reaction cross section at low proton kinetic energy.

The observation of solar neutrinos began in 1970 in the pioneering radiochemical detector employing ^{37}Cl as the target for the reaction $\nu_e+{}^{37}\text{Cl}\rightarrow{}^{37}\text{Ar}+e^-$. The corrected average rate of ν_e interactions in the detector during a 20-year data-taking interval [6] is between 0.3 [7] and 0.4 [8] times the value predicted by the SSM. The ^{37}Cl detector and the data obtained from it, including a possible neutrino flux variation with time [9], are discussed more fully in later sections of this paper.

B. The Kamiokande II solar-neutrino experiment

For 20 years no experiment either confirmed or extended the result of the ^{37}Cl experiment. However, since the beginning of 1986, Kamiokande II (Kamiokande II is an acronym for the Kamioka Nucleon Decay Experiment in its second version), an imaging water Čerenkov detector, has been operating with an electron energy threshold which makes it sensitive to part (roughly one-half) of the ^{8}B solar-neutrino spectrum. Solar neutrinos are detected in this detector through neutrino-electron elastic scattering, $\nu_e e\rightarrow\nu_e e$, and measurement of the initial position and vector momentum of the recoiling electron. The kinematics of the elastic scattering imposes an angular constraint on the recoiling electron:

$$\cos\theta_e=\frac{1+m_e/E_\nu}{(1+2m_e/T_e)^{1/2}}\ , \tag{1}$$

where θ_e is the scattering angle, m_e is the mass of electron, E_ν is the energy of the incident neutrino, and T_e is the kinetic energy of the recoil electron. The scattering angle θ_e is small ($\theta_e^2\le 2m_e/T_e$), so that the incident neutrino direction is largely preserved in the recoiling electron direction. The detector has an angular resolution of 28° at 10 MeV, mainly limited by multiple scattering of the electron in the water, and therefore makes it possible to point the incident neutrinos back to the Sun, if indeed that is their origin. In addition, the observed electrons yield information on the energy spectrum of the incident ν_e, and on the real time of each event, which is crucial for studying possible time variations of the ^{8}B solar-neutrino flux and neutrino oscillations.

The solar-neutrino data from Kamiokande II yield a clear directional correlation of the solar-neutrino-induced electron events with respect to the Sun and a measurement of the differential electron total energy distribution. In this paper, we present a fuller explanation of the experimental method and of the solar-neutrino analysis than published before [10] and the results of an analysis based on 1040 days of data. In Sec. II we describe in detail the properties of the Kamiokande II detector. Calibration procedures are presented in Sec. III, and backgrounds discussed in Sec. IV. Data analysis is described in Sec. V, and results and comparison with the ^{37}Cl results are given in Sec. VI. Section VII briefly states the conclusions.

II. KAMIOKANDE II DETECTOR

A. Detector

Kamiokande II is an imaging water Čerenkov detector located 1000 m underground [2700 m.w.e. (meters of water equivalent)] in the Kamioka metal mine in the Gifu prefecture of Japan, at 36.4° N, 137.3° E, and 25.8° N geomagnetic latitude.

The Kamiokande II detector consists of an inner main detector and an outer anticounter. A schematic view of the detector is shown in Fig. 1. The inner main detector is contained in a cylindrical steel tank and has a cylindrical volume, 14.4 m in diameter $\times$13.1 m in height, containing 2142 metric tons of water. A total of 948 photomultiplier tubes (PMT's), each with 50-cm ϕ photosensitive area, cover 20% of the entire inner surface of the water tank. The fiducial mass for the ^{8}B solar-neutrino measurement is 680 tons, with boundaries 2.0 m (3.14 m) from the barrel and the bottom wall (the top wall).

B. Anticounter

A 4π solid-angle anticounter surrounding the main detector is a water Čerenkov counter of total mass 1800

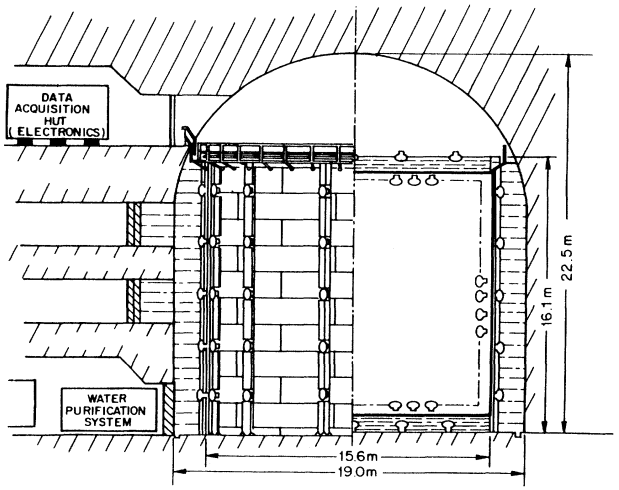

FIG. 1. Schematic drawing of the Kamiokande II detector showing the location of the water purification system, anticounter, and electronics hut.

metric tons with 123 (50-cm ϕ) PMT's (21 on the bottom, 22 on the top, and 80 on the barrel) to detect any signals outside the main detector volume and to shield against γ rays and neutrons from outside the detector. The entire inner surface of the anticounter sections is covered by aluminum sheets to obtain good light collection efficiency. The mean thickness of water in the anticounter is 1.2, 0.8, and 1.7 m for the bottom, top, and barrel sections, respectively. The top and bottom regions of the anticounter are within the main detector tank optically separated from the main detector by black plastic sheets. The anticounter protecting the barrel of the main detector was constructed by water-sealing the cavity holding the main detector and filling it with water.

C. Water and air purification

There are several reasons for operating an elaborate water purification system: (1) The water transparency should be maintained at a high, constant value (attenuation length $\gtrsim 35$ m) to minimize the loss of Čerenkov photons. Since metal ions, such as Fe^{++}, Ni^{++}, and Co^{++}, and organic molecules such as bacteria decrease water transparency because of their absorptivity, the water must be continually circulated through a purification system, even though the relatively low temperature ($\sim 11\,^{\circ}C$) of the water helps to prevent proliferation of bacteria. (2) At low energies the trigger rate is dominated by radioisotopes present in the detector water. The removal of radioactivity in the water is one of the most important functions of the purification system. Special modifications were added to the water purification system to remove heavy radioactive elements from the tank water. The level of radioactivity has been low enough to allow solar-neutrino data to be taken since January 1987. Furthermore, air-tightening of the detector itself and of the water purification system, part of which was in place by the spring of 1987, reduced the radioactive background from radon in the air dissolving in the water of the detector.

The water purification system consists of the following elements as shown in Fig. 2 (the water flow direction is denoted by arrows): (a) 5 membrane filters; (b) a degasifier; (c) an ultraviolet sterilizer to destroy bacteria; (d) ion-exchange columns for removing uranium (CR-55); (e) a mixed-bed-type deionization system; and (f) pumps. The water is circulated through the bottom anticounter, the inner detector, the top anticounter, and the purification system, and the flow rate is 4.5 tons/h.

This system has maintained the uranium and radium content in the tank water at less than 10^{-3} pCi liter, and reduced the equilibrium radon content of the water by a factor of 10^3 relative to the water in the mine.

D. Electronics and data acquisition

The Kamiokande II electronics is designed to implement multihit time and charge measurement for all PMT's in the main detector and the anticounter, and to allow new trigger configurations to be set for a variety of physical events. The circuitry reduces the dead time of the system to nearly the limits imposed by the PMT's recovery times (less than 50 nsec), and increases the ability of the detector to record a large number of burst events without loss of information.

The electronics is illustrated in the block diagram in Fig. 3. The electronics system is organized into 272 boards of front end cards, each of which processes four channels of signals, with sixteen such boards to a crate. Each crate for the main detector (total fifteen crates) contains one trigger processing card and one control card. Each crate for the anticounter (total two crates) contains only a control card. The anticounter information is only used off line. The control continuously cycles through the channels in the crate searching for flags indicating the presence of signals to be digitized. When a channel flag is recognized, the time and charge are digitized and stored along with the event number in a 512-word-deep first-in–first-out (FIFO) memory on the control card. When the event trigger (see next section) occurs, the time (20 nsec least count) and the event numbers are established

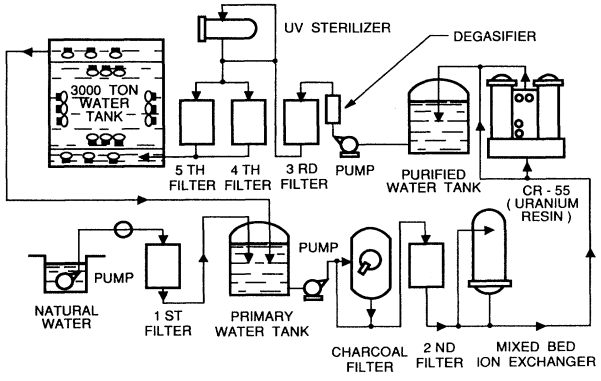

FIG. 2. Block diagram of the Kamiokande II water purification system.

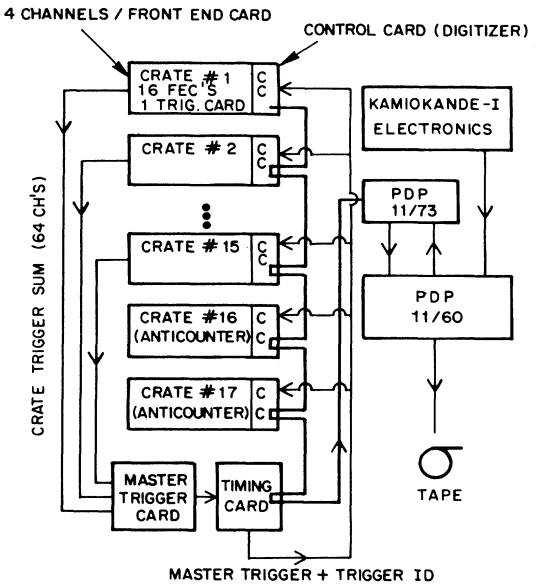

FIG. 3. Block diagram of the Kamiokande II electronics.

by a timing card. A PDP 11/73 computer reads the time, and drains the FIFO memories in each control card of the digitized PMT information until all of the memories in the seventeen crates are empty. The PDP 11/73 sorts the information into event buffers. A PDP 11/60 (replaced by a micro-Vax early in 1989) then reads the information from the 11/73 and records the data on magnetic tape.

E. Event trigger and trigger efficiency

The Kamiokande II trigger system is designed to collect all events above approximately 6 MeV with almost no dead time. If the PMT signal after passing through an amplifier is above the threshold of approximately 0.35 photoelectron, which is controlled by the PDP 11/73, a rectangular discriminator output of ~ 100 nsec width and ~ 5 mV height is produced and transmitted over the backplane of a crate to the trigger card in the same crate. The trigger card in each crate of the main detector sums the 64 channels of discriminator outputs to make an analog pulse, and the master trigger card finally sums the outputs from the 15 trigger cards. An event trigger is generated when the peak value of the final analog pulse is above the trigger threshold which is adjustable and set to 112 mV, effectively corresponding to ~ 17 hit PMT at the single photoelectron level. The trigger threshold was lowered to 100 mV in October 1987 to take advantage of low trigger rate; then it was changed again to 112 mV in June 1988 when the PMT gain was doubled. It should be noted that the anticounter information does not participate in the event trigger formation, but it is useful to veto events coming from outside, e.g., cosmic-ray muons, γ rays, and neutrons, in the off-line data reduction and analysis.

The trigger efficiency as a function of total energy is obtained from Monte Carlo–generated electron events. The initial trigger accepted 7.6 MeV (10.0 MeV) electrons with 50% (90%) efficiency over the 680-metric-ton fiducial volume of the detector with a trigger threshold of 112 mV. After October 1987 and before the PMT gain change in June 1988, the trigger accepted 6.7 (9.2)MeV electrons with 50(90%) efficiency over the fiducial volume with 100-mV trigger threshold. After the PMT gain increase the efficiencies became 50% for 6.1-MeV electrons and 90% for 9.0-MeV electrons over the fiducial volume. (After the end of May, 1989, an additional trigger which was lower than the immediately earlier one by 15% was also employed. But the present analysis was performed only for the data taken with the 6.1-MeV threshold.) The trigger efficiency as a function of energy is shown in Fig. 4. The time dependence of the trigger threshold (50% efficiency) is shown in Fig. 5. The total rate of triggers in the detector was, for example since May 1989, ~ 5 Hz at 5.2 MeV and ~ 1 Hz at 6.1 MeV threshold, of which 0.37 Hz is due to cosmic-ray muons. The remaining trigger rate is presumably due to radioactivity in the water of the inner counter and in the detector materials. One of the possible radioactive sources is the β decay of ^{214}Bi (β spectrum end-point energy 3.26 MeV), a daughter of ^{222}Rn.

III. CALIBRATION

To observe solar neutrinos in a detector such as Kamiokande II, it is important to calculate accurately the true energy, interaction position, and direction of an event. The PMT timing information and the Čerenkov pattern of an event are vital for reconstruction of the interaction (vertex) position and direction of low-energy electrons. The energy of low-energy electrons is estimated using the number of hit PMT's. Accordingly, accurate calibrations of individual channels and of the overall response are necessary.

A. Energy measurement and calibration

Single low-energy electrons scattered by neutrinos incident on the detector cause the emission of Čerenkov light with a total intensity nearly proportional to the total energy of the charged particles. In the energy range

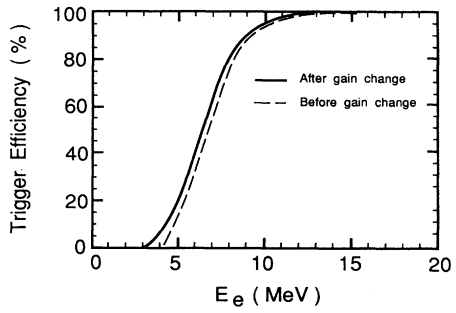

FIG. 4. Plot of trigger efficiency against total electron energy before and after the gain change. The fiducial mass for the solar-neutrino measurement is 680 tons.

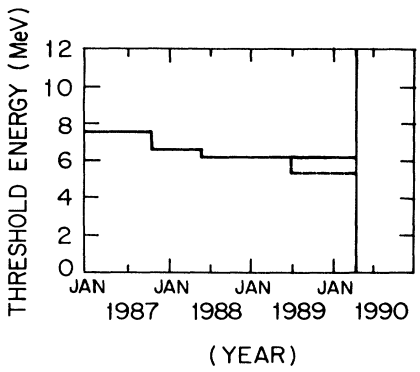

FIG. 5. Dependence of the electron energy threshold on time during the period January, 1987 through April, 1990, indicating the improvement in sensitivity in that period. After May 1989, two different energy thresholds are shown (see text).

of the events discussed here (≤ 15 MeV), a typical PMT response corresponds to the detection of one photoelectron. Thus, the energy of low-energy electrons can be estimated by an appropriate sum of the number of PMT's which respond to the signal.

The actual response of the detector to the Čerenkov light depends on attenuation of the Čerenkov light by absorption in the water and the geometrical effects arising from event location and the location of the responding PMT's. The number of hit PMT's corrected for these effects is expressed by the effective number of hit PMT's ($N_{\rm eff}$), which is described in detail in Appendix A.

An electron of 10-MeV total energy gives an average 26 and 30 $N_{\rm eff}$ before and after gain doubling, respectively. Thus, the total electron energy, E_e in MeV, of each event is estimated simply by dividing $N_{\rm eff}$ by 2.6 (3.0) for the data before (after) gain doubling.

The energy calibration of the detector is performed using three independent methods. The first method uses γ rays from a Ni thermal neutron capture reaction [Ni(n,γ)Ni*]. The second method makes use of the continuous energy distribution of decay electrons from stopping cosmic-ray muons. The third method makes use of the β spectra of radioactive nuclei (end-point energies of 10–17 MeV) which are produced by spallation induced by cosmic-ray muons.

1. *Cf-Ni 9-MeV γ-ray source*

γ rays of energies about 9 MeV are emitted from the thermal neutron capture reaction by nickel, Ni(n,γ)Ni*. The γ rays are produced in transitions with total emitted energies 9.0, 7.8, and 6.8 MeV, and relative intensities of 0.71, 0.16, and 0.13, respectively, where these values are the products of the mass fraction and cross section for thermal neutron capture for each nickel isotope [11]. The calibration system utilizes ^{252}Cf as a neutron source, which is enclosed by a water-filled nickel can with dimensions of 9.5 cm in diameter, 16 cm in height, and 1 mm in thickness. The amount of ^{252}Cf is 97 μCi in activity and it emits 4.6×10^5 neutrons/sec at $\sim$2 MeV which are slowed by interactions with the water in the nickel can.

Since ^{252}Cf itself emits γ rays, two sets of data were taken: one with ^{252}Cf only (without a nickel can) and the other with ^{252}Cf and Ni. The measured $N_{\rm eff}$ distributions of γ rays for both data sets are shown in Fig. 6. The $N_{\rm eff}$ spectrum of γ rays from the neutron capture reaction in Ni is obtained by subtraction, and is shown in Fig. 7. The Monte Carlo simulation was tuned to reproduce the peak of the $N_{\rm eff}$ distribution of the ^{252}Cf/Ni calibration data within $\pm1\%$.

The shape of the observed spectrum in Fig. 7, especially the width which represents the energy resolution, is well reproduced by the Monte Carlo simulation. The calibration was also performed by placing the source at various places in the detector fiducial volume other than the center. The Monte Carlo simulation reproduces the peak position of the spectrum within $\pm2\%$ for these additional calibration data. The stability of the gain of the detector was monitored using the γ-ray source. The relative gain of the detector monitored with the Ni(n,γ)Ni* source is shown in Fig. 8. The gain is stable within $\pm2\%$ over four years of operation from 1987 to 1990.

2. *Stopping-muon decays*

Electrons from stopping-muon decays are sampled and compared with a Monte Carlo simulation of the well-known muon decay (Michel) spectrum. Comparison of the $N_{\rm eff}$ distribution is shown in Fig. 9 and yields

$$\frac{\text{Monte Carlo simulation}}{\text{Data}} = 1.011\pm0.003 \ . \qquad (2)$$

3. *Spallation events*

β decays from cosmic-ray muon-induced spallation products were obtained in conjunction with the information of the preceding muons.

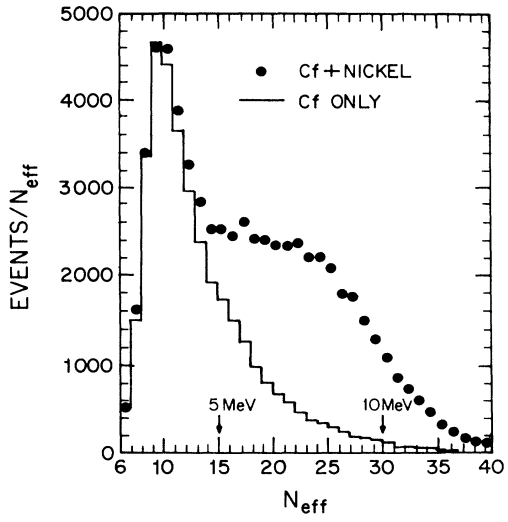

FIG. 6. The measured γ-ray spectra from the Cf + Ni (data points) and Cf (solid histogram) sources.

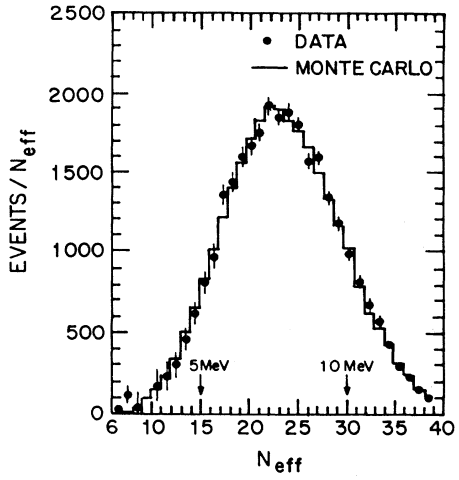

FIG. 7. The observed γ-ray spectrum from Ni(n,γ)Ni* obtained by subtraction of the Cf spectrum from the Cf+Ni spectrum in Fig. 6. The solid histogram is the Monte Carlo calculated spectrum from Ni(n,γ)Ni*.

Monte Carlo events were generated to simulate the β decay of the short-lived isotopes, ^{12}B ($\tau_{1/2}=20.3$ msec, $E_{\max}=13.37$ MeV) and ^{12}N ($\tau_{1/2}=11.0$ msec, $E_{\max}=16.38$ MeV) in the ratio ^{12}B to ^{12}N, 0.85:0.15, which accounted for an observed half-life of 18.4 ± 0.8 msec shown in Fig. 10. Comparison of the observed N_{eff} distribution of β rays from the short-lived isotopes and the adjusted Monte Carlo simulation, shown in Fig. 11, gives

$$\frac{\text{Monte Carlo simulation}}{\text{Data}}=0.98\pm0.01\ . \tag{3}$$

4. *Energy calibration, energy resolution, and angular resolution*

Combining the results of the three independent energy calibrations, one obtains

$$\frac{\text{Monte Carlo simulation}}{\text{Data}}=1.00\pm\lesssim0.03\ . \tag{4}$$

From the consistency of the three calibration results, the uncertainty in the absolute energy calibration is estimated to be less than 3%. The energy resolution for low-energy electrons is shown in Fig. 12 before and after the gain change. Typical values of $\sigma(E_e)/E_e$ after the gain change are 21% at 8.5 MeV, 20% at 10.0 MeV, and 18% at 15.0 MeV. The energy resolution after the gain change is approximated by the following empirical formula (this approximation is correct below $E_e<12$ MeV):

$$\sigma(E_e)/E_e=0.63/\sqrt{E_e}\ , \tag{5}$$

where E_e is the electron total energy in MeV.

The angular resolution of the detector was calibrated using a collimator with the Ni(n,γ)Ni* source placed at the top of the detector. The observed data are compared with the Monte Carlo simulation in Fig. 13. The angular resolution of the detector is limited by multiple Coulomb

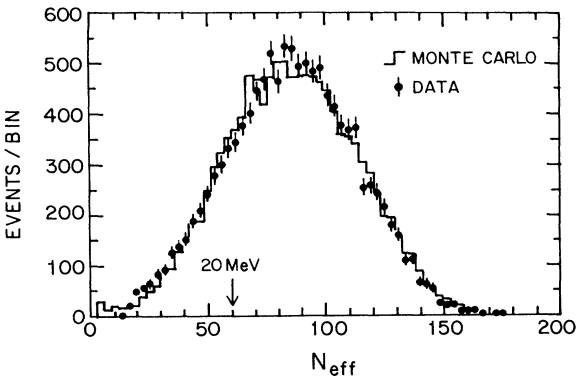

FIG. 9. Distribution in N_{eff} of electrons from stopping muons (data points) compared with that of the Monte Carlo simulation (histogram) which includes energy resolution.

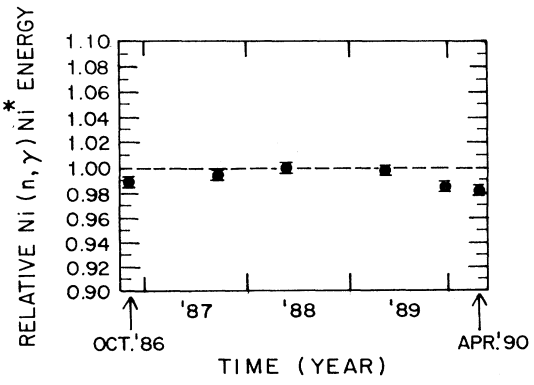

FIG. 8. Plot of the gain stability, i.e., the relative value of the Ni(n,γ)Ni* calibration source in the interval between October, 1986 and April, 1990, showing less than 2% change in that time period.

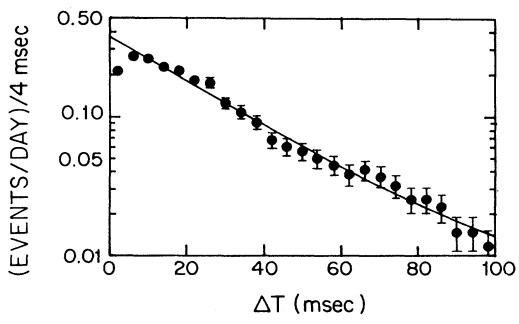

FIG. 10. Plot of event rate against time interval ΔT from the preceding muon event. The solid curve is the lifetime obtained from a mixture of short-lived spallation β decaying products ^{12}B and ^{12}N. Spallation products with energy threshold of 10 MeV accompanied by preceding muons with pulse height above 20 000 p.e. were selected.

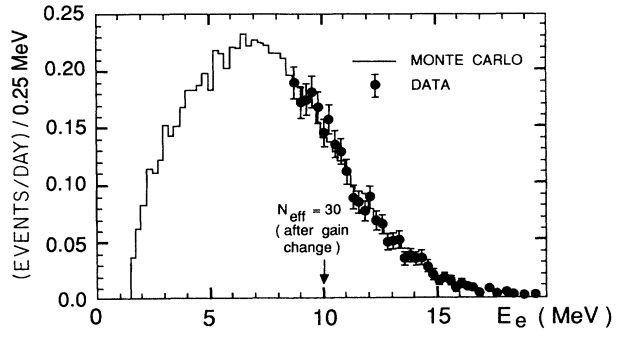

FIG. 11. Distribution in E_e (energy in MeV) of the β decays from the short-lived spallation products. Also shown is the Monte Carlo–simulated spectrum of β decays from a mixture of ^{12}B and ^{12}N with a relative ratio of 0.85 to 0.15 for $E_e \geq 10$ MeV consistent with the lifetime plot in Fig. 10. Data and energy calibration taken before and after the gain change.

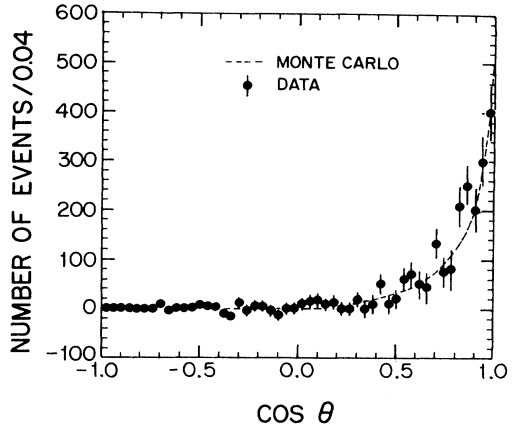

FIG. 13. Measured distribution in $\cos\theta$ of collimated γ rays compared with that of the Monte Carlo simulation. The angle θ is the angle between the reconstructed electron direction and the downward direction (see text).

scattering of electrons. Therefore, this calibration tests the validity of the simulation of the propagation of electrons and γ's in water, for which we adopted EGS version 4 [12]. The dependence of the electron angular resolution on electron energy is shown in Fig. 14 before and after the gain change.

B. Timing calibration

The timing calibration corrects for the variation of time response as a function of pulse amplitude, for the time delay due to the different high voltage applied to the PMT, and for the different cable lengths for the individual channels so that overall time synchronization may be achieved. The synchronization is described by calibration constants associated with the electronics and other constants associated with the remainder of the detector.

The timing calibration is achieved by a laser system which utilizes a nitrogen gas laser as a light source. Upon receiving a trigger, the laser emits a light pulse with a wavelength of 337 nm for less than 3-nsec duration. A quartz plate splits the light pulse into two: one goes to PIN diodes for the electronics trigger, and the other goes through a 6-bit attenuator. A combination of six attenuator components changes the intensity of light from a few tenths of a single photoelectron to a few hundreds of photoelectrons in the tank PMT. The laser light is guided along a long optical fiber to a diffusing ball which makes the light reasonably isotropic. Timing calibration data are taken with the diffusing ball at the center of the detector to synchronize all PMT channels. Data to calibrate the electronics alone are taken by activating the discriminator of each channel with a test pulse from the timing card, and by stopping the activation with a delayed global trigger.

The time response as a function of pulse height is obtained from the calibration data for each individual PMT channel. Timing calibration constants are calculated by determining the characteristic function for each obtained time response as a function of pulse height.

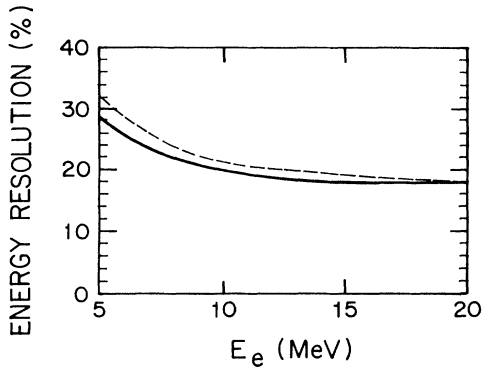

FIG. 12. Energy resolution plotted vs total electron energy obtained by the Monte Carlo calculations before (dashed) and after (solid) gain change.

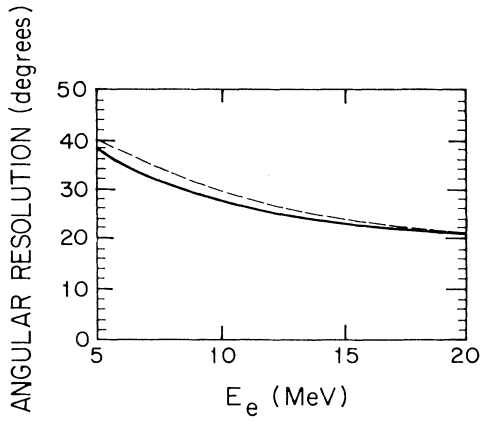

FIG. 14. Angular resolution as a function of total electron energy before (dashed) and after (solid) gain change.

C. Calibration of vertex position resolution

The track length of a 10-MeV electron is about 5 cm, and therefore it is almost pointlike in the detector. The origin of an electron event is determined by reconstructing the vertex of the Čerenkov cone utilizing the relative timing and pulse-height information from each struck PMT.

From the best estimated vertex position, the time residual of each responding PMT was calculated by subtracting the time of flight from the measured time. Figure 15(a) shows the time residual distribution of an event, sharply peaked at zero when a correct vertex position is found. On the other hand, an incorrect vertex position leads to a broad time residual distribution as shown in Fig. 15(b).

The vertex position resolution was calibrated by γ rays from the Ni(n,γ)Ni* source. The data were taken with the calibration source at the center of the water tank and at other positions in the fiducial volume which gave the same results. The position of the source was well reproduced by the mean of the reconstructed vertex positions within 10 cm in each coordinate and the 1σ deviation was identical in each coordinate as well as consistent with a Monte Carlo simulation. No systematic bias was found in the vertex reconstruction.

The vertex position resolution was obtained from the 1σ deviation of the reconstructed vertex positions relative to the location of the source. The measured vertex position resolution of γ rays is shown in Fig. 16(a) as a function of energy, and is compared with that of the Monte Carlo simulation. However, the vertex position resolution in Fig. 16(a) is for γ rays, and thus it is worse than the one for electrons because of the conversion length of γ rays in water ($\sim$40 cm). The Monte Carlo simulation using EGS4 [12] tuned for the γ-ray calibration data was used to estimate the vertex resolution of electrons. The vertex position resolution shown in Fig. 16(b), thus obtained, is 1.2 and 1.0 m for 10-MeV electrons for the data before and after the gain change, respectively.

D. Expected signature

The neutrino energy spectrum of ^{8}B decay is precisely determined [13], and precise measurements of elec-

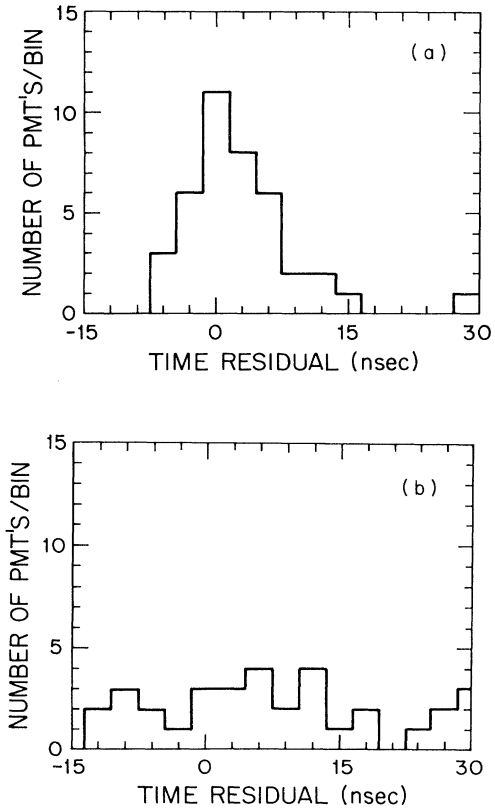

FIG. 15. (a) Distribution of the number of PMT's per unit of time residual against the residual time for a typical well reconstructed event. If all the measured times of the PMT's in an event are properly corrected for the time of flight from a correct vertex position, the distribution should peak sharply at the mean time residual as shown. (b) Same as (a) but for an event with an incorrect vertex position.

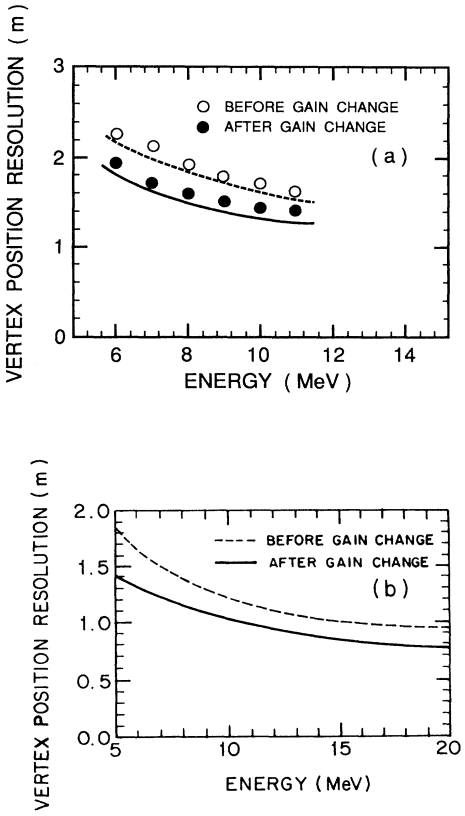

FIG. 16. (a) The points show the measured vertex position resolution (1σ) of γ rays from the Ni source against total energy before and after the gain change compared with the Monte Carlo–simulated resolutions. In plotting resolution against energy in MeV, the N_{eff} distributions corresponding to given energies in MeV were taken into account. (b) Vertex position resolution of electrons from the Monte Carlo simulation before (dashed) and after (solid) the gain change.

troweak parameters provide the cross section of $\nu e \rightarrow \nu e$ scattering accurately. Thus, the shape of the energy distribution of the final-state electrons may be calculated precisely. The energy distribution is shown in Fig. 17(a). The response of the detector is obtained from a Monte Carlo simulation, in which the detailed detector structure is taken into account. The resultant expected energy distribution, in which the detector response is convoluted, is shown in Fig. 17(b) for the data after the gain change. The difference in expected energy distribution between the data before and after the gain change is small, and is taken into account in the data analysis. The expected event rate is 0.86 (events/day)/680 tons for $E_e \geq 7.5$ MeV, and 0.28(0.29) (events/day)/680 tons for $E_e \geq 10$ MeV after (before) gain doubling, when the calculation of Bahcall and Ulrich [7] is used, and 35% lower for the calculation of Turck-Chièze *et al.* [8]. The slight decrease ($<3\%$) in the event rate after the gain change is due to the improvement in the energy resolution and the reduction of background.

IV. BACKGROUND

The main backgrounds in the solar-neutrino measurement in Kamiokande II are from natural radioactivity in the detector water, from γ rays and neutrons emanating from the rock surrounding the detector, and from the β decays of the muon-induced spallation nuclei in the water.

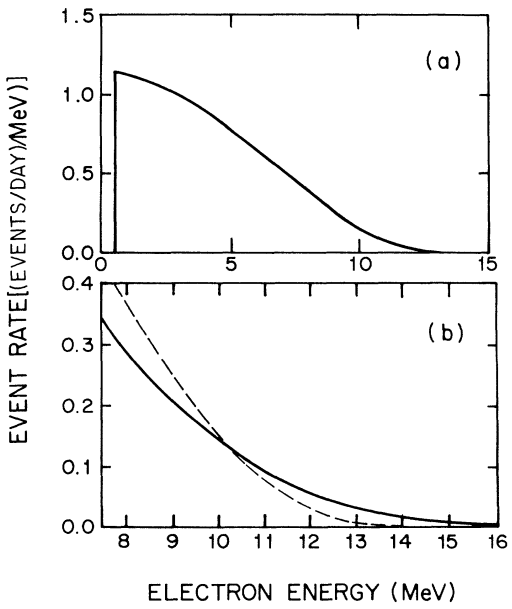

FIG. 17. (a) Total energy spectrum of electrons from $\nu_e e \rightarrow \nu_e e$ based on the laboratory measured flux $\phi_\nu(^8\mathrm{B})$ and the cross section for $\nu_e e \rightarrow \nu_e e$. (b) Monte Carlo simulation of the expected total electron energy spectrum in the Kamiokande II detector after the gain change (solid line). The difference in expected energy distribution between before and after the gain change is small, and is taken into account in the data analysis. The dashed line is same as (a), but for the corresponding energy region.

A. Radioactivity in the tank water

At low energies ($\lesssim 7$ MeV) most of the trigger rate is due to the β decay of ^{214}Bi [β spectrum end point 3.26 MeV, a daughter of ^{222}Rn ($\tau_{1/2}=3.8$d)]. Although the maximum energy of the β spectrum is below the trigger threshold, the detection of low-energy electrons from ^{214}Bi decay results from the convolution of the energy resolution of the detector with a fractional event acceptance between 10^{-5} and 10^{-4}.

The origins of the ^{222}Rn are known. (1) It is primarily contained in the water of the mine (estimated radon content: 200~300 pCi/liter). The presence of the ^{222}Rn is confirmed by the observation of a sudden rise in the trigger rate when fresh water is added to the tank, followed by a reduction of the trigger rate consistent with the 3.8-d half-life. (2) It is dissolved in the detector water from the air. The concentration of radon in the air inside the Kamioka mine is ~50 pCi/liter, which is at least 100 times higher than that of the air outside the mine. (3) It is also produced from the decay of ^{226}Ra in the detector water.

Special modifications were added to the water purification system to remove heavy radioactive elements from the tank water. In April 1986, an ion-exchange column was installed to remove the uranium selectively by utilizing a chelate resin. The uranium content in the circulating water was 0.17 pCi/liter initially, and became less than 10^{-3} pCi/liter by December 1986. To remove ^{226}Ra as well as other metal ions, another ion-exchange column was installed. The ^{226}Ra content in the primary water is 1.5×10^{-2} pCi/liter and the content in the circulating water was reduced to less than 10^{-3} pCi/liter. The top of the water tank was sealed in the spring of 1987, and the water circulation/purification system was made airtight to prevent radon in the air in the cavity from entering the water. In addition, radon-free gas has been supplied to both the main tank and the buffer tanks in the purification system since the middle of 1987, with the aim of having the pressure of this gas balance the pressure of the outside air and thereby compensate for air leaks in the system. A degasification system was also installed to remove air (radon) from the circulating water.

The trigger rate due to the β decay of ^{214}Bi has been substantially reduced by the above efforts to eliminate radioactivity in the water. As a result, the trigger threshold has been lowered several times, to be finally set at 5.2 MeV. The final event rate in the 680-ton fiducial volume is ~5 events/day for $E_e \geq 7.5$ MeV, as can be seen in Fig. 19. A sharp rise of the background below 7 MeV is not completely understood, although the prime suspect is ^{222}Rn probably from incomplete air tightening.

γ rays from spontaneous fission of uranium is one source of radioactive background. Uranium in the inner detector water was further reduced, using the chelate resin, to the level $\lesssim 2.4\times10^{-4}$ pCi/liter, which corresponds to $\lesssim 0.05$ (events/day)/680 tons for $E_e \geq 7.5$ MeV.

B. γ rays from the rock

The flux of external γ rays from the surrounding rock was measured to be $\sim 3\times10^5$ per day per all surface of

the detector for $E_e \geq 7.5$ MeV. The anticounter layer reduces the flux by ~ 3 orders of magnitude, and the remaining external γ rays convert in the inner detector. Most remaining γ rays have vertex positions near the surface of the detector. They are reduced by an additional factor of ~ 400 by limiting events to the fiducial volume and by the γ-ray cut (see Sec. V E). The resultant background of external γ rays is $1 \sim 2$ (events/day)/680 tons ($E_e \geq 7.5$ MeV) in the solar-neutrino analysis.

C. Spallation products of cosmic-ray muons

Cosmic-ray muons produce radioactive nuclides in the detector water leading to β decays with lifetimes of a few tens of milliseconds to several seconds by the following processes: (1) direct fragmentation of target oxygen nuclei; (2) capture by oxygen of π^- (arising from inelastic interactions of the muons with water) can contribute to the production of radioactive nuclides, e.g., $\pi^- + {}^{16}\mathrm{O} \rightarrow {}^{12}\mathrm{B} + \alpha$, $\pi^- + {}^{16}\mathrm{O} \rightarrow {}^{12}\mathrm{N} + 4n$, and so on; (3) nuclear capture of stopping μ^- in oxygen nuclei occasionally leads to ^{16}N which is radioactive: $\mu^- + {}^{16}\mathrm{O} \rightarrow {}^{16}\mathrm{N} + \nu_\mu$, ${}^{16}\mathrm{N} \rightarrow {}^{16}\mathrm{O} + \beta^- + \bar{\nu}_e$ ($\tau_{1/2} = 7.13$ sec). The event rate of these processes is observed to be ~ 20 (events/day)/680 tons ($E_e \geq 7.5$ MeV) at the incident cosmic-ray muon rate of 0.37 Hz. Most of the nuclei are produced along the track of muons. Furthermore, the preceding muons are usually accompanied by an energetic nuclear or electromagnetic cascade shower. Using these characteristics, this background can be reduced by a factor of 10–20, as will be described in Sec. V D.

Process (3) can be determined precisely as giving rise to ~ 0.3 (events/day)/680 tons with $E_e \geq 7.5$ MeV. The decay of ^{16}N produces a β ray and γ ray, which deposit an energy of ~ 10 MeV total. This background is reduced by a factor of ~ 10 using the timing and spatial correlation between stopping μ^- and low-energy events. Therefore, the contribution to the solar-neutrino background is negligible.

In addition to the relatively long-lived β decaying spallation products, low-energy electron events are observed with a decay time structure of $\tau = 2.27 \pm 0.03$ μsec; the energy spectrum of these events is consistent with the muon decay (Michel) spectrum and the decay time structure is consistent with the decay lifetime of μ^+ in water. These fast followers are another result of $\pi^\pm$ production by inelastic muon interactions in water; essentially all π^- are captured by oxygen nuclei leading to β-decaying nuclei, while most π^+ decay into μ^+. The π^0 contribute to the shower attending the incident muon.

The $\bar{\nu}_e$ flux from nuclear reactors was calculated by Lagage [14] in 1985 to be $\sim (1.6 \times 10^6 \bar{\nu}_e/\mathrm{cm}^2)$/sec at Kamioka. The $\bar{\nu}_e$ is absorbed by a free proton in the detector with emission of a positron. The total production rate of positrons is calculated to be 1.5 (events/day)/680 tons. Because of the soft energy spectrum of the $\bar{\nu}_e$, the expected event rate above 7.5 MeV is only 0.02 to 0.03 (events/day)/680 tons.

Finally, note that all the backgrounds described above have isotropic angular distributions with respect to the direction of the Sun. Taking into account the directional information, the background rate can be further reduced by a factor ~ 10.

V. DATA ANALYSIS

The Kamiokande II detector began operating at the beginning of 1986. However, the radioactive background was too high and too variable to permit observation of solar neutrinos until December 1986. Measurement of ^{8}B solar neutrinos was carried out on 1040 detector live days of data with low radioactivity background, taken from January 1987 through April 1990.

Two independent off-line analyses were performed on the data. Each analysis obtained a final sample using independent programs for event reconstruction and applying different event-selection criteria.

A. Event selection

The selection of events was done in several steps: (i) data reduction, (ii) vertex reconstruction and fiducial volume cut, (iii) elimination of muon-induced background, and (iv) remaining γ-ray cut. The data reduction step rejects cosmic rays and selects events contained in the inner detector. The vertex positions of the reduced data are reconstructed and most external γ rays are rejected by the fiducial volume cut. Most of the remaining high-energy ($\gtrsim 8$ MeV) events are the β decays of spallation products. These events are rejected using spatial and time information. A fraction of the external γ rays remain even after the fiducial volume cut. The fourth step therefore imposes a tighter criterion to reduce the remaining γ rays. The details of each step are described in this section.

B. Data reduction

Data which satisfy the following criteria are selected: (1) an anticounter total pulse height ≤ 30 p.e. (photoelectrons); (2) a time difference from the previous event ≥ 100 μ sec; (3) main detector total pulse height ≤ 100 p.e. (corresponds to $E_e \lesssim 30$ MeV). Criterion (1) rejects cosmic-ray muons. The probability that an event contained in the inner detector will have an anticounter signal greater than 30 p.e. due to accidental noise is much less than 10^{-3}. Criterion (2) rejects decay electrons from stopping muons. The loss of the ^{8}B solar-neutrino signal by this criterion is (100×10^{-6}) sec $\times (1-5)$ Hz $= 10^{-4} - 5 \times 10^{-4}$, where the second factor is the typical trigger rate. Criterion (3) limits the energy range for events accepted as solar neutrinos.

C. Vertex reconstruction and fiducial volume cut

The vertex position of each event is determined using the timing information and Čerenkov pattern of fired PMT's. The principle of vertex reconstruction is to find the position where the width of the histogram of residual time (t_i minus time of flight from vertex to PMT$_i$, where t_i is the measured time in PMT$_i$) is minimal and the spatial distribution of the fired PMT's fits well to the expect-

ed Čerenkov pattern. Particle direction is also determined from the Čerenkov pattern information. The vertex position distribution of the reduced events is shown in Fig. 18, where the horizontal axis, R^2, is the square of the radial coordinate and the vertical axis is the vertical coordinate Z. This distribution shows that events accumulate at the periphery of the detector, especially near the top. The physical boundary of the cylindrical main detector is defined by -5.94 m $\leq Z \leq 7.14$ m and $R \leq 7.22$ m. The different event rates near the top, barrel, and bottom walls are due to different thicknesses of the anticounter on those regions: top, 0.8 m; barrel, 1.7 m; bottom, 1.2 m, and therefore different levels of γ-ray absorption. Most of these γ rays were rejected by limiting the fiducial volume for the solar-neutrino measurement to 680 tons, which was chosen to be 3.14 m below the top PMT layer, and 2 m inside the barrel and bottom PMT layers, i.e., $|Z| \leq 4.0$ m and $R \leq 5.22$ m, as shown in Fig. 18. The energy spectra of events in the total detector volume and in the fiducial volume are shown by open and closed circles, respectively, in Fig. 19. The fiducial volume cut reduces the number of events by a factor of ~ 10, where the ratio of fiducial to detector volume (2140 tons) is 0.32. Most of events with $E_e \gtrsim 17$ meV in the total detector volume are due to $\mu \rightarrow e$ decay electrons whose preceding muons stop near the wall without emitting Čerenkov light in the detector. They are also rejected through the fiducial volume cut.

The integral event rate after the fiducial volume cut was, for example, 14 (20) events/day for $E_e \geq 8.5$ MeV and 6 (7) events/day for $E_e \geq 10.0$ MeV after (before) the gain change. The low-energy event rate in the fiducial volume was reduced after the gain change for the following reasons: (1) improvement of the energy resolution suppressed the contribution of radioactive nuclei; (2) the increase of the number hit PMT in an event led to improvement in vertex reconstruction, which eliminated many less well reconstructed events at the edge of the fiducial volume. The same fiducial volume cut was imposed in the two independent analyses based on independent programs for event reconstruction and independently obtained calibration constants.

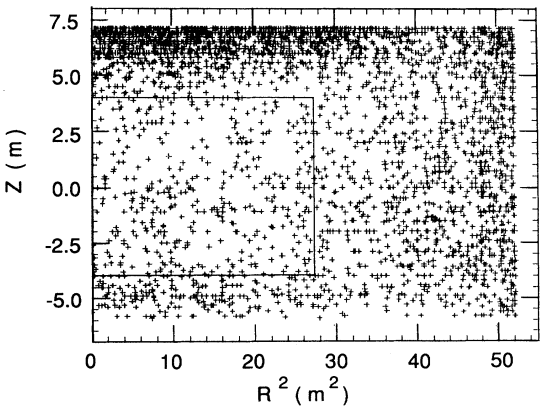

FIG. 18. Distribution in Z (vertical dimension) vs R^2 (radial dimension squared) of reconstructed event vertices showing excesses of events at the top and the periphery of the barrel. The solid inner boundary is the outline of the fiducial volume.

D. Elimination of muon-induced background

A major background remaining after the fiducial volume cut is β decays from spallation products (see Sec. IV C). To determine the criteria for removing this background, the characteristics of these events were studied in detail. The time interval ΔT distribution between low-energy events and the preceding muon for events with $E_e \geq 10$ MeV was shown in Fig. 10 which exhibited a half-life of 18.4 ± 0.8 msec. As noted earlier, the preced-

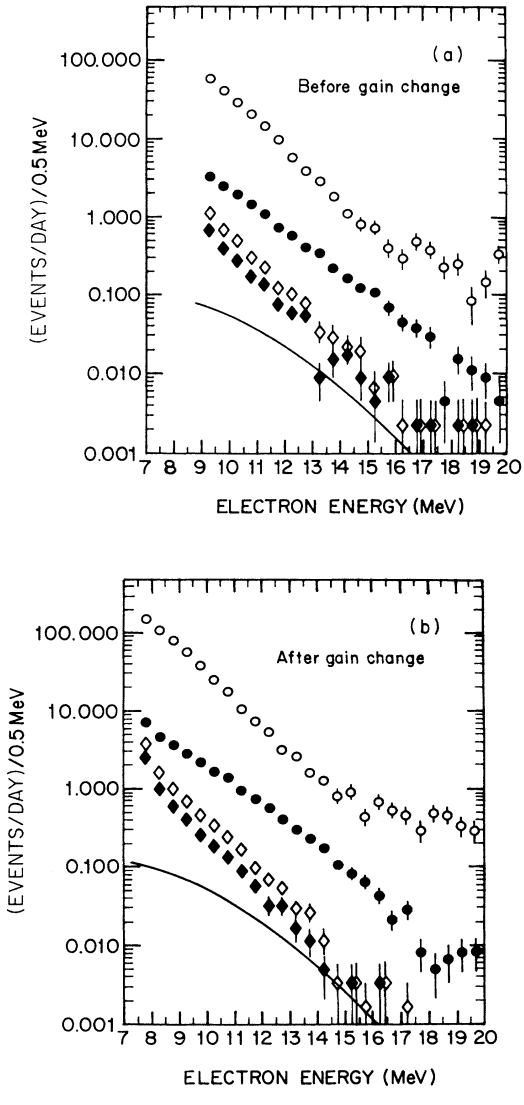

FIG. 19. Trigger (event) rates as a function of total electron energy for all events (○), events in the fiducial volume (●), fiducial volume events after the spallation cut (◇), and after the remaining γ-ray cut (◆): (a) before the gain change, (b) after the gain change. The curve shows the expected event rate for the ^{8}B neutrinos calculated with SSM in Ref. [7].

ing muons usually create energetic nuclear or electromagnetic showers. Consequently, the total pulse-height distribution of the preceding muons is much larger than that of typical through-going muons, as shown in Fig. 20. The spatial correlation, ΔR, between the vertex position of low-energy events and the track of the preceding muons is shown in Fig. 21, (a) for events with $E_e \geq 9$ MeV, $0.1 \leq \Delta T < 100$ msec, (b) for events with $\Delta T < 100$ μsec. These figures indicate that the background induced by spallation is correlated in time and space with relatively high pulse-height muons. Nuclei with longer lifetimes are also observed. Figure 22 shows the ΔT distribution of low-energy events ($E_e \geq 10$ MeV) with $\Delta R \leq 3$ m relative to muon tracks with pulse height $\geq 40\,000$ p.e. An admixture of the β decays of ^{8}Li($\tau_{1/2}=0.84$ sec), ^{8}B($\tau_{1/2}=0.77$ sec), and ^{16}N($\tau_{1/2}=7.13$ sec) seems to be observed.

To eliminate most β decays two types of criteria were utilized in the two independent analyses. In the first, events were rejected if they had a small time gap (ΔT) from and spatial correlation (ΔR) with preceding muons accompanied by energetic showers. Figure 23 illustrates the criteria using the plot of pulse height of preceding muon vs ΔT. Low-energy events in region 1 are rejected without any restriction on ΔR. Events in regions 2 and 3 are rejected if they have spatial correlation $\Delta R \leq 3$ m and $\Delta R \leq 2$ m, respectively. These criteria were determined to maximize a figure of merit defined by $(1-\epsilon)/\sqrt{N}$, where ϵ is the dead time of the cut, and N is the number of events remaining after the cut. The dead time of the above criteria is 15.3%. With a probability of $\sim 14\%$ relative to single spallation low-energy events, multiple low-energy events can also be induced by a single muon as shown in Fig. 24. For multiple spallation events, the following criterion is applied: if a muon is marked by the above criteria as causing at least one spallation event,

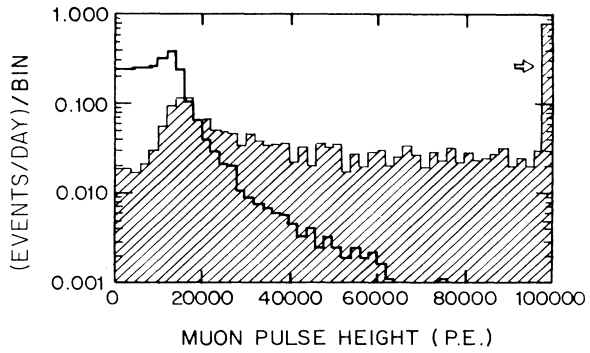

FIG. 20. Muon event rate per observed pulse-height interval against pulse height in total photoelectrons. The cross-hatched area shows the pulse-height distribution of the initiators of spallation events, which satisfy the requirement of the time interval to the spallation events ($E_e \geq 10$ MeV) to be less than 50 msec. The right arrow shows that the last bin is the sum of all events above 10^5 p.e. The histogram gives the shape of the distribution for all muons traversing the Kamiokande II detector. The number of events contained in the histogram is scaled to the number of events in the cross-hatched area.

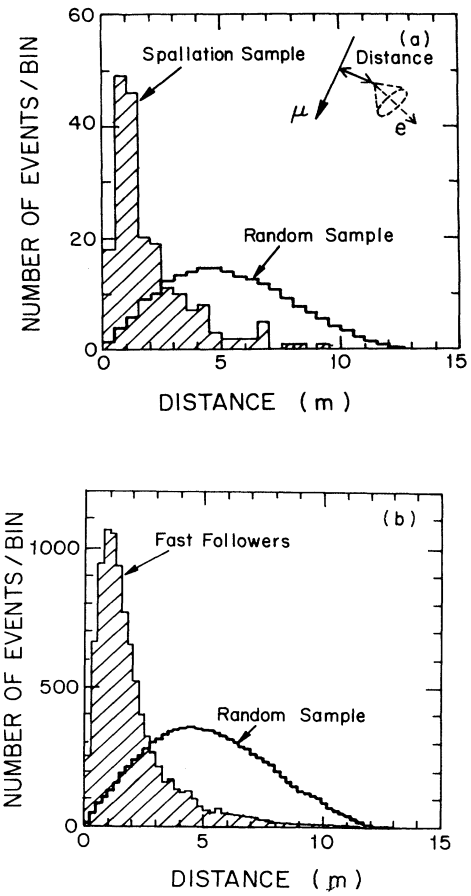

FIG. 21. (a) Distance correlation of the vertices of low-energy events from spallation products with the track of the initiating muon. The narrow distribution (cross hatched) is for spallation β decays. The broad distribution is for a random sample of low-energy events. (b) Distance correlation of fast followers, i.e., events occurring in time interval $\Delta T < 100$ msec after an incident muon (presumably the result of the $\pi^+ \rightarrow \mu^+ \rightarrow e^+$ decay chain), with respect to the track of the initiating muon.

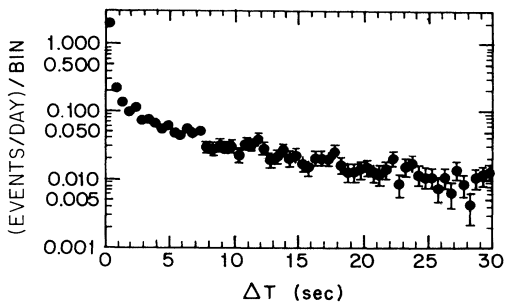

FIG. 22. Time distribution of long-lived β-decaying spallation products with $\Delta R \leq 3$ m ($E_e \geq 10$ MeV). A pulse height above 40 000 p.e. was required for the preceding muons.

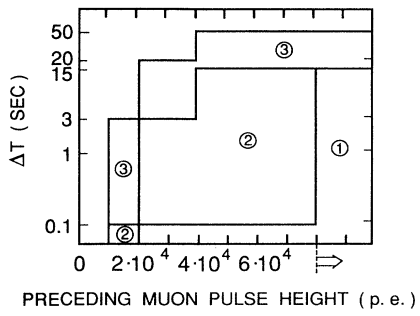

FIG. 23. Plot of the time interval ΔT vs the pulse height of the preceding muon to show the cuts imposed on spallation products. For details, see text.

then events in the time interval 50 sec directly after the muon are vetoed. The dead time of this additional criterion is 1.5%.

The background of ^{16}N induced by stopping cosmic-ray muons is removed using the spatial (ΔR) and timing (ΔT) correlation with stopping muons, where ΔR is the distance between the vertex position of a low-energy event and the final position of the preceding stopping muon. The ΔR distribution of events with $\Delta T \leq 20$ sec is compared with that of chance coincidence in Fig. 25. A clear spatial correlation is seen at small ΔR, and events which correlate as $\Delta R \leq 3$ m and $\Delta T \leq 20$ sec are rejected. The dead time of this criterion is 0.14%.

The energy spectrum after the elimination of muon-induced background is shown by open diamonds in Fig. 19. These cuts reduced the event rate above 10 MeV by a factor of ~ 5. The total dead time was 16.9%. The rejection efficiency for the selection criteria shown in Fig. 23 was estimated by the detailed study of the timing and distance correlation with preceding muons and pulse-height information on the muons. The rejection efficiency of the muon-induced background is estimated to be $\sim 95\%$.

In the second type of criteria, an effort was made to utilize only event times and thereby lessen to some extent reliance on the Monte Carlo simulation. The requirements imposed were that (a) the time of any low-energy event relative to the time of the previous cosmic-ray muon event with pulse height greater than 10^4 p.e. (4×10^4 p.e.) be greater than 100 msec (20 sec), and (b) low-energy events in the fiducial volume were removed which occurred within 40 sec of each other without reference to a preceding muon. Requirement (b) is based on the data in Fig. 26, and is effective because multiple pions are produced in the cascade attending an inelastic muon interaction, frequently leading to more than one low-energy decay event (a cluster) within the 40-sec interval. These criteria of the second type reduced the low-energy ($E_e \geq 10$ MeV) event sample by a factor of 4.4, and introduced a dead time of 16.7%. The rejection efficiency was approximately 90%.

The resultant energy spectrum of low-energy events after applying the fiducial volume cut and the spallation event criteria of the second type is similar in all respects to the corresponding spectrum in Fig. 19. That spectrum mostly consists of the remnants of the two original components. The soft component is due to the residual radioactivity, and the hard component is due to spallation products and external γ rays which are not completely el-

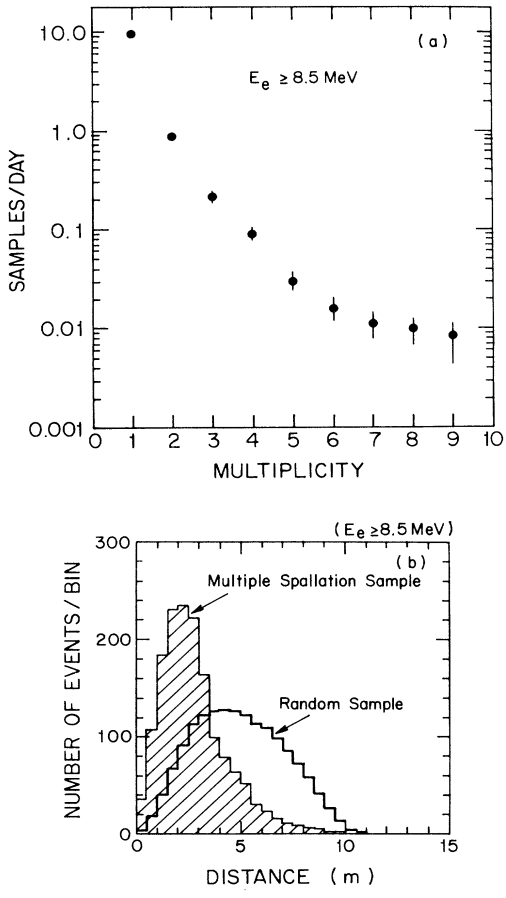

FIG. 24. (a) Distribution of numbers of spallation events per day having a given multiplicity of observed β-decaying nuclei. ($E_e \geq 8.5$ MeV.) (b) Internal space correlation of the vertices of low-energy events comprising the multiple spallation sample. The random sample is shown for contrast.

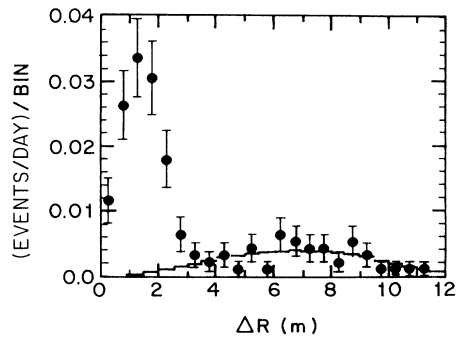

FIG. 25. Plot showing the correlation in space of the β decays ($E_e \geq 9.3$ MeV) from the long-lived ($\sim$7-sec) ^{16}N isotope with the incident muon track ($\Delta T \leq 20$ sec). The histogram is for a randomly chosen sample of low-energy events.

iminated by the event-selection criteria described above. To reduce the contribution of the soft component to the background in the solar-neutrino analysis, we used only the data sample with $E_e \geq 9.3$ MeV before the gain change described above, and with $E_e \geq 7.5$ MeV after the gain change.

E. Remaining γ-ray cut

One background remaining after the rejection of the muon-induced background is due to external γ rays which reconstructed poorly at the boundary of the fiducial volume. These may be identified using position and direction information. Figure 27(a) shows a two-dimensional plot of the Z coordinate of the reconstructed vertex position versus cosine of zenith angle. One can see an excess of events directed inwards, i.e., upward (downward)-going events near the bottom (top) of the detector. An excess is also observed in a plot of R^2 vs $\cos\theta_{\rm wall}$ as shown in Fig. 27(b), where $\cos\theta_{\rm wall}$ is the cosine of the angle between the electron direction and the normal to the nearest wall. To reduce this background, events were rejected which had vertex positions near the edge of the fiducial volume (outer 1-m layer) and $\cos\theta_{\rm wall} > 0.67$. This cut further reduced the event rate by $\sim 40\%$, and introduced additional dead time of 13% estimated by the Monte Carlo simulation. The resultant event rate as a function of electron energy after this cut is shown as the solid diamonds in Fig. 19.

To test whether the γ-ray cut was biased by the directional criteria, the event-selection process was repeated with various smaller fiducial volumes without the γ-ray cut. Within statistical errors, the observed solar-neutrino signals were the same as the corresponding result for the larger (680-ton) fiducial region with γ-ray cut. The dead time of the γ-ray cut is independently confirmed by using spallation event sample. In addition, final results for the solar-neutrino flux and electron energy distribution were also obtained without the remaining γ-ray cut. Results with and without the remaining γ-ray cut were completely consistent.

To extract the ^{8}B solar-neutrino signal, the final event sample was tested for a directional correlation with respect to the Sun. The test provides an additional order of magnitude discrimination against the isotropic background, which is described in the next section.

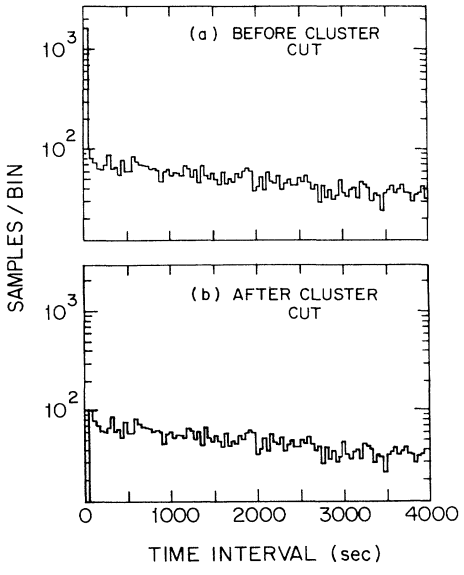

FIG. 26. Distributions of the time interval between two adjacent low-energy events ($E_e \geq 8.5$ MeV) in the 680-ton fiducial volume: (a) before cluster cut, (b) after cluster cut (see text).

VI. RESULTS

A. Directional correlation with the Sun and electron energy distribution

Any correlation of the direction of observed low-energy events with the direction from the Sun to Earth is made possible by the preservation of the incident ν_e direction in the reaction $\nu_e e \rightarrow \nu_e e$, the moderate angle of multiple scattering of the recoiling electrons, and the observation in real time of each low-energy event, which

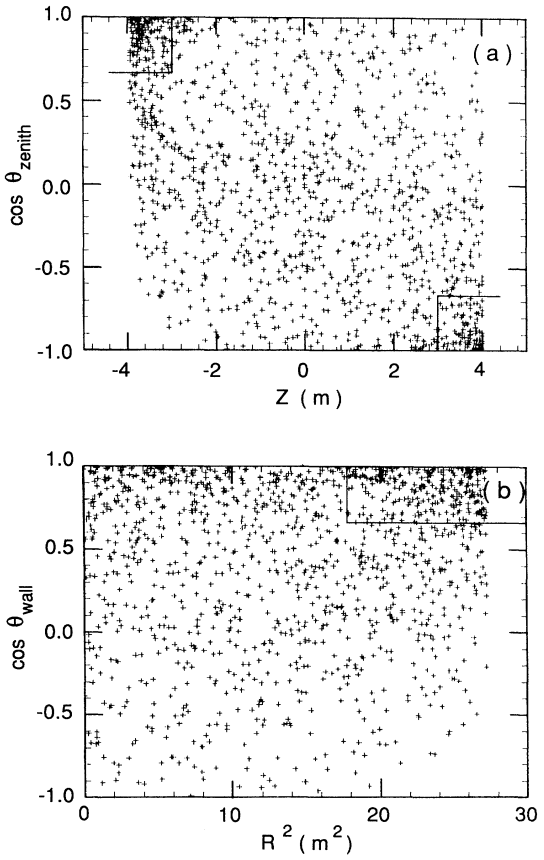

FIG. 27. (a) Plot of the cosine of the zenith angle vs the z direction for low-energy events ($E_e \geq 10$ MeV) after the spallation cut. (b) Plot of the cosine of the angle between the normal to the nearest tank wall and the electron direction as a function of R^2 for the events in (a). The regions indicated by the boxes show the remaining γ cut.

permits the correlation of the Sun's position in the sky relative to the detector coordinates at a given instant.

Figure 28(a) shows the distribution in $\cos\theta_\odot$ for $E_e \geq 9.3$ MeV for the entire 1040-day data sample. ($\cos\theta_\odot = 1$ corresponds to the direction from the Sun to Earth.) The distributions for the data samples before and after the gain doubling are separately shown in Figs. 28(b) and 28(c). Figure 28(d) shows the distribution for $E_e \geq 7.5$ MeV after the gain change. The solid histograms in the figures give the shape of the signal expected from a Monte Carlo simulation based on the angular and energy resolution of the detector. For simplicity, we have made the area under the solid histograms in Fig. 28 equal to the prediction of the SSM calculation of Bahcall and Ulrich [7], and have also done this in certain subsequent figures. Where the numerical value of the SSM prediction is not a basis for comparison we use the symbol "SSM." All angular distributions show enhancement in the direction from the Sun above the isotropic background. However, the amount of the enhancement is less than that expected from calculations [7,8] based on the SSM.

The intensity of the signal relative to the SSM was obtained by the χ^2 method and by a maximum-likelihood method with results differing by only a few percent. The likelihood function was defined by

$$L(x) = \prod_i \{\tfrac{1}{2}[1-\alpha(E_{e,i})x] + f_{\text{solar}}(\cos\theta_{\odot,i})\alpha(E_{e,i})x\} \tag{6}$$

with

$$\alpha(E_{e,i}) = N_{\text{SSM}}(E_{e,i})/N_{\text{data}}(E_{e,i}) ,$$

where $N_{\text{data}}(E_e)$ and $N_{\text{SSM}}(E_e)$ are energy distributions of the final data sample and expected signal from SSM. $f_{\text{solar}}(\cos\theta_\odot)$ is a normalized function which represents an expected angular distribution of the signal. The parameter x gives the intensity of the signal relative to the SSM prediction. The first term in $L(x)$ represents the isotropic background.

The energy spectrum of the final-state electrons induced by the solar ν_e was obtained by performing a maximum-likelihood fit using events in each energy bin, and also by a direct subtraction method in which the energy distribution of the isotropic background ($\cos\theta_\odot < 0.8$) was subtracted from the energy distribution of the events with $\cos\theta_\odot \geq 0.90$. The resultant spectrum was essentially identical for both methods, and is shown in Fig. 29 relative to the simulated spectrum based on $\sigma(\nu_e e \rightarrow \nu_e e)$, the known shape of the ν_e spectrum from ^{8}B decay, and the energy resolution of the detector. The best-fit spectrum (dashed histogram) yields 0.46 SSM [7] with reduced χ^2 of 1.05. The shapes of the data and the histogram in Fig. 29 are independent of the total flux prediction of the SSM.

We note that the shape of the background (events with $\cos\theta_\odot < 0.8$) electron energy distribution was compared with the shape of the background subtracted signal distribution in Fig. 29(a) by means of a χ^2 test. The test yielded a confidence level $< 1\%$ on the probability that the

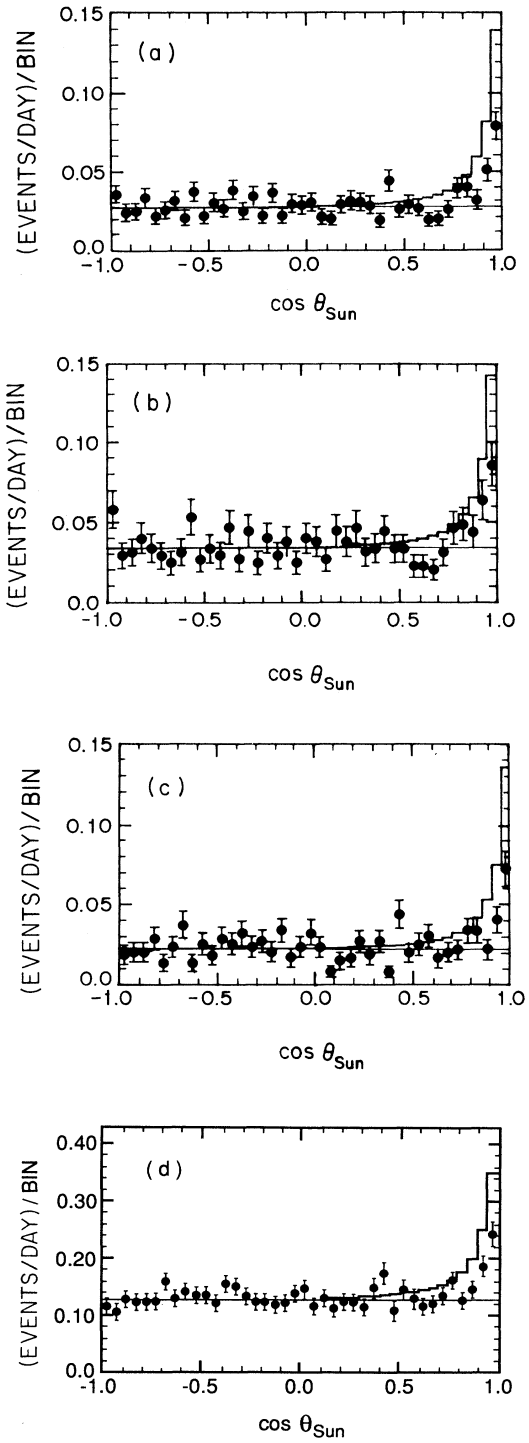

FIG. 28. (a) Plot of the cosine of the angle between the electron direction and a radius vector from the Sun showing the signal from the Sun plus an isotropic background. This plot is for $E_e \geq 9.3$ MeV, and the time period January, 1987 through April, 1990, a total of 1040 live-detector days. (b) Same as (a) but for the period January, 1987 through May, 1988, a total 450 live-detector days. (c) Same as (a) but for the period June, 1988 through April, 1990, a total 590 live-detector days. (d) Same as (c) but for $E_e \geq 7.5$ MeV. The solid histograms give the shape of the signal expected from a Monte Carlo simulation (see text).

signal and background spectral shapes are the same.

The data samples of the two analyses were carefully compared in many ways after each step in the analyses. Based on the sample after the fiducial volume cut, the correlations in event reconstruction and energy estimation between the two analyses were tested and showed excellent agreement. The distributions in $\cos\theta_\odot$ and in electron energy obtained from the two analyses are essentially the same, as are the resultant values of the solar-neutrino flux. This is shown in Fig. 30 which gives the $\cos\theta_\odot$ and electron energy distributions for the final data samples from the independent analysis to be compared with the distributions in Figs. 28(a) and 29(a).

B. Solar-neutrino flux measurement

Measurement of the solar-neutrino signal was carried out based on 1040 days of data sample, consisting of subsamples of 450 days (January 1987 through May 1988) at $E_e \geq 9.3$ MeV and 590 days (June 1988 through April 1990) at $E_e \geq 7.5$ MeV. The flux value for the combined 450-day and 590-day data sample is

$$\text{Data/SSM} = 0.46 \pm 0.05(\text{stat}) \pm 0.06(\text{syst.})$$

(SSM from [7]),

and

$$\text{Data / SSM} = 0.70 \pm 0.08(\text{stat}) \pm 0.09(\text{syst})$$

(SSM from [8]).

There is no significant difference between the relative flux values of the 450- and 590-day samples, which are $0.48 \pm 0.09(\text{stat}) \pm 0.08(\text{syst})$ [$0.73 \pm 0.14(\text{stat}) \pm 0.12(\text{syst})$] ($E_e \geq 9.3$ MeV), January 1987 through May 1988; and $0.45 \pm 0.06(\text{stat}) \pm 0.06(\text{syst})$ [$0.68 \pm 0.09(\text{stat}) \pm 0.09$ (syst)] ($E_e \geq 7.5$ MeV), June 1988 through April 1990, respectively.

Moreover, the ^{8}B solar-neutrino signal in Kamiokande II is observed in the $\cos\theta_\odot$ distribution with only a fiducial volume cut on the reduced data. This is shown in Fig. 31 which compares the values of Data/"SSM" after the application of each cut on the data. The statistical error becomes smaller as the successive cuts are applied but the central value is essentially constant in Fig. 31.

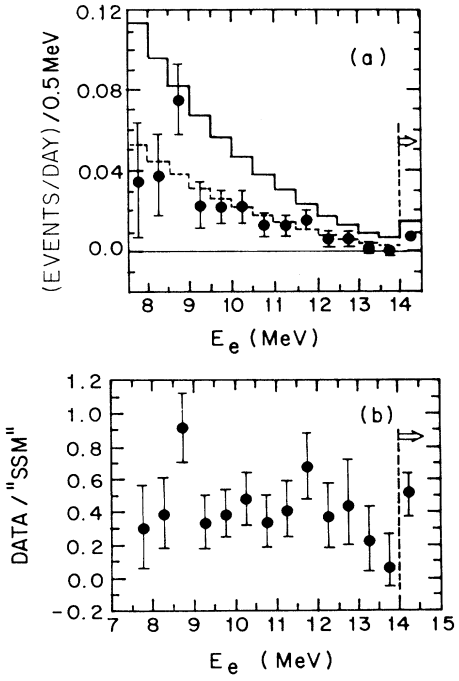

FIG. 29. (a) Differential electron total energy distribution of the events produced by ^{8}B solar neutrinos. The point in the interval above 14 MeV is the sum of all events above 14 MeV. The dashed histogram is the best fit to the data of a Monte Carlo calculation based on $\sigma(\nu_e e \rightarrow \nu_e e)$, the known shape of the neutrino flux from ^{8}B decay, and the energy resolution of the detector. The solid histogram has the area predicted by the SSM of Bahcall and Ulrich [7]. (b) The flux value relative to the SSM [7] as a function of E_e. This plot shows the stability of the solar-neutrino signal with electron energy, and is not dependent on the total flux prediction of the SSM, which is consequently indicated by "SSM."

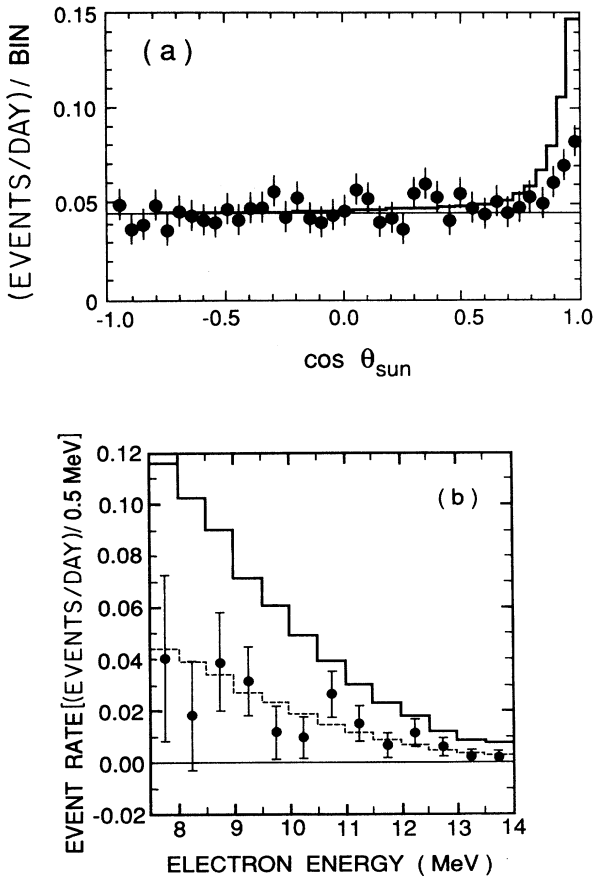

FIG. 30. (a) Same as the plot in Fig. 28(a) but from the independent analysis described in the text. (b) Same as the plot in Fig. 29(a) but from the independent analysis described in the text.

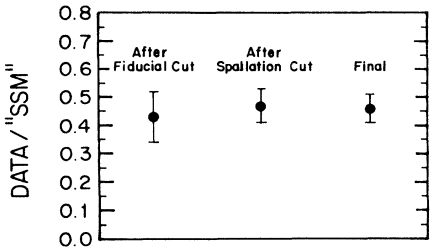

FIG. 31. Plot showing the stability of the relative flux value after the application of the different event-selection criteria. Note that a numerical result consistent with the final result is obtained after only a fiducial volume cut.

The possible sources of systematic error in the flux determination are uncertainties in absolute energy calibration, in angular resolution, and in the calculated dead time of various cuts. The uncertainty in the absolute energy calibration is estimated to be 3%, as described in Sec. II, which corresponds to 12% of the obtained flux. The uncertainty in the measurement of the angular resolution is less that 20%, which corresponds to 7% of the obtained flux. The dead time and uncertainty introduced by the various event-selection criteria are estimated using a Monte Carlo simulation based on real data of known physical processes, such as spallation products. The estimated uncertainty is 4% of the measured flux. The quadratic sum of the above uncertainties is 14% of the obtained flux, which corresponds to $0.06\times$SSM if we adopt the SSM in [7].

We remark that the value of the ^{8}B solar-neutrino flux, relative to the prediction of the SSM, can be obtained straightforwardly, if less precisely, from the $\cos\theta_\odot$ distribution in Fig. 28(a), without resorting to the maximum-likelihood analysis. A direct, but imprecise, way is to sum the data points (signal) in, say, the five bins nearest $\cos\theta_\odot=1$, and also the SSM prediction for those bins; the ratio Data/SSM for the specified electron energy threshold follows immediately after subtraction of the summed isotropic background in those bins. The procedure is refined and made more precise by considering each data point in a given interval of $\cos\theta_\odot$ with its statistical error as an independent measurement relative to the SSM prediction for that $\cos\theta_\odot$ interval and extracting the weighted average of Data/SSM and the resultant error on the weighted average. The error found in the more precise method is approximately one-half that from the summing procedure, the reduction coming from the high signal rate in the two bins above $\cos\theta_\odot=0.9$. Both methods utilize the semiempirical knowledge of the shape of the expected $\cos\theta_\odot$ distribution dominated principally by multiple scattering along the recoiling electron trajectory and the corresponding measured angular resolution of the detector (Sec. III A 4). The events generated in the Monte Carlo simulation according to that angular prescription are then subjected to the identical event-selection criteria as the data, so that the ratio Data/SSM is largely independent of systematic uncertainties. However, the uncertainty in the measured angular resolution is included in the estimated systematic error (Sec. VI A). In practice, the value of Data/SSM and its statistical error are calculated as described in Sec. VI A, and given immediately above.

Note also that the absolute total number of signal events can also be obtained by extrapolating the number of events in the last five bins along the predicted shape of the $\cos\theta_\odot$ distribution to include all of the expected signal. This extrapolation amounts to an increase of approximately 20% over the signal observed in the last five bins of the $\cos\theta_\odot$ distribution, the uncertainty of which is included in the quoted statistical and systematic errors. The correction for dead time is also necessary to find the correct absolute total number of events, and is included in the Monte Carlo simulation.

C. Time variation

The flux of solar neutrinos is predicted to be stable over several million years, because the neutrinos are produced in the deep interior of the Sun. Consequently, if a time variation were to be observed on a time scale of several years, it could be ascribed to neutrino properties, such as a neutrino magnetic moment or neutrino mass and mixing. The Kamiokande II data are of particular interest in this connection because the data-taking time extends over a period in which sunspot activity, reflecting the solar magnetic cycle, rose steeply from a minimum value at the end of solar magnetic cycle 21 to maximum value approximately 15 times larger at the peak of solar cycle 22, as shown in Fig. 32.

Accordingly, it is possible to test for a correlation of the ^{8}B solar-neutrino yield with the sunspot activity by comparing the relative flux values obtained when the total data sample is divided into shorter time intervals. The time variation of the ^{8}B solar-neutrino flux is shown in Fig. 33(a) in which the data are separated into five time intervals, each of approximately 200 live detector days, where the electron energy threshold is 9.3 and 7.5 MeV for the data before and after the gain change (June 1988), respectively. To avoid a possible energy threshold dependence of the flux, the time variation with a common energy threshold (9.3 MeV) is also shown in Fig. 33(b). The source of the point-to-point systematic error is the possible time variation of the detector gain. As shown in Fig.

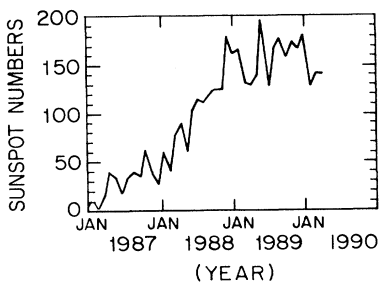

FIG. 32. Plot of sunspot number vs time in the period 1987–1990 (April).

8 the gain of the detector was stable within ±2%, which corresponds to ±8% in the measured flux value. Thus, the systematic error is smaller than the statistical error on each point in Fig. 33. The reduced χ^2 calculated under the assumption of constant flux with respect to time is 0.25 and 0.40 for the mixed [Fig. 33(a)] and common [Fig. 33(b)] energy thresholds, respectively, which correspond to 90% and 81% C.L.

Other possible short-time variations of the neutrino flux, such as day-night, seasonal, and semiannual variations, are also of interest because they might be indications of neutrino oscillations or of a solar magnetic field effect. The negative results of searches for these variations in the Kamiokande II data are described in detail elsewhere [15], as are the negative results of searches for a neutrino burst in a short time interval correlated with a solar flare [16].

D. Flux comparison with ^{37}Cl detector

The observation of solar neutrinos was initiated in about 1970, in a detector utilizing ^{37}Cl as the neutrino target for the reaction, $\nu_e + {}^{37}\mathrm{Cl} \rightarrow {}^{37}\mathrm{Ar} + e^-$, with a neutrino energy threshold of 0.814 MeV [6]. The detector, which is still taking data, is located 1480-m-deep underground in the Homestake Gold Mine in South Dakota, and consists of 610 tons of perchloroethylene (C_2Cl_4) containing 133 tons of ^{37}Cl. The produced ^{37}Ar, with half-life of 35 days, is removed from the target vessel with better than 90% efficiency by flushing the perchloroethylene with helium gas approximately 5 or 6 times per year. The ^{37}Ar is then separated from the helium in a series of traps, and counted in a proportional ionization counter in which the 2.8-keV Auger electrons accompanying ^{37}Ar electron capture decay are detected with 40–45 % efficiency. The ^{37}Cl experiment is especially sensitive to the 0.86-MeV monoenergetic ν_e from the electron capture reaction of ^{7}Be ($e^- + {}^7\mathrm{Be} \rightarrow {}^7\mathrm{Li} + \nu_e$), and to the 0–15-MeV neutrino spectrum from the decay of ^{8}B ($^8\mathrm{B} \rightarrow {}^8\mathrm{Be}^* + e^+ + \nu_e$) in the Sun. The average corrected total rate of ν_e interactions in the detector from 1970 to 1988 was 2.3±0.3 solar-neutrino units (SNU) (or 0.43±0.05 ^{37}Ar atoms/day), where a solar-neutrino unit is 10^{-36} interactions per target atom per second [6]. The discrepancy between the value of 2.3±0.3 SNU from the ^{37}Cl experiment and the values of 7.9±2.6(3σ) SNU [7] and 5.8±1.3(1σ) SNU [8] predicted by the SSM has persisted for more than a decade, and is often referred to as the solar-neutrino problem. The suggestion in the ^{37}Cl data that the count rate might be anticorrelated with solar activity has added further interest to the problem [9].

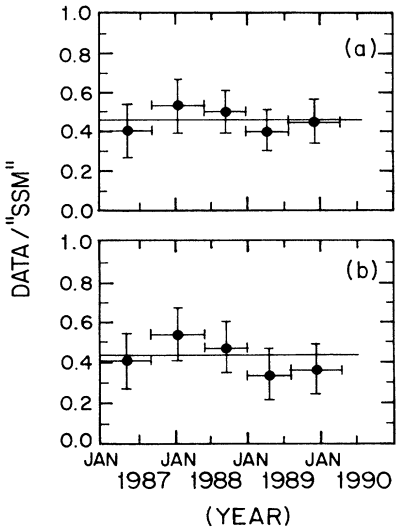

FIG. 33. (a) Plot of the solar neutrino flux in five time intervals each of approximately 200 days from January, 1987 through April, 1990. The earliest two points are with $E_e \geq 9.3$ MeV, and the latest three points are with $E_e \geq 7.5$ MeV (after the gain change). (b) Same as (a) but all points are with $E_e \geq 9.3$ MeV. The horizontal lines are the best fits assuming no time variation with reduced χ^2's of 0.25 and 0.40 for (a) and (b), respectively.

The capture rate in the ^{37}Cl detector averaged over the data from 1970 through 1990 is reported to be 2.3±0.3 SNU [6], which corresponds to 0.29±0.04 relative to the SSM calculation of [7] (7.9 SNU), and 0.40±0.05 relative to the calculation of [8] (5.8 SNU). During the period January, 1987 through April, 1990, the weighted average of the ^{37}Cl data is 2.12±0.34 SNU. The SSM predicts that 6.1 SNU (4.0 SNU) is contributed by ^{8}B neutrinos in each of those calculations. The other important source of solar neutrinos in the ^{37}Cl detector is from ^{7}Be production: 1.1 SNU at 0.861 MeV energy in both calculations, with relatively small uncertainty.

Consequently, using the Kamiokande II result which indicates (0.46×6.1 [7] = 0.70×4.0 [8]) = 2.8 SNU for the ^{8}B contribution in the capture rate, and assuming the ^{7}Be contribution, the capture rate in the ^{37}Cl experiment during the period January, 1987 through April, 1990, should be at least 3.9 SNU from ^{8}B and ^{7}Be sources alone. (An additional 0.6 SNU is expected from other sources of low-energy neutrinos: ^{13}N, ^{15}O, and the *pep* reaction.) Thus, it is difficult to explain the results of both the Kamiokande II and ^{37}Cl detectors (assuming both are correct) by manipulating the solar model. This, in turn, suggests that some as yet undetected intrinsic property of neutrinos might be playing a role in the solar-neutrino deficit.

E. Time variation comparison with ^{37}Cl detector

During the period January, 1987 through April, 1990, both detectors were taking data, and it is possible to compare the flux measurements of each as a function of time in that interval. This involves some ambiguity, since the SSM predicts that 0.23 [7] (0.31 [8]) of the flux to which the ^{37}Cl detector is sensitive is due to other sources than ^{8}B, i.e., ^{7}Be and *pep* neutrinos, and the neutrinos from CNO cycle. These energies are below the energy threshold for observation by the Kamiokande II detector. However, it seems simplest at present to compare observed rates in the two detectors directly without attempts at correction or normalization. This is done in

Fig. 34, where are shown the ^{37}Cl results for each individual extraction during the period January, 1987 through April, 1990, and the Kamiokande II data in that time interval. The plotted ^{37}Cl values of Data/SSM are the measured values in SNU divided by 7.9 SNU [7]. To facilitate comparison between the two data sets, several of the ^{37}Cl runs corresponding in time with the appropriate Kamiokande II data point have been averaged $[\sum_i(S_i/\sigma_i^2)/\sum_i(1/\sigma_i^2)$, where S_i is the value for the ith run], and the averages shown as the cross-hatched boxes in Fig. 34. No significant disagreement exists between the two data sets shown in Fig. 34, other than the difference between the points in the last half of 1988, and no compelling evidence for a time variation in the time period plotted is presented in either data set [17].

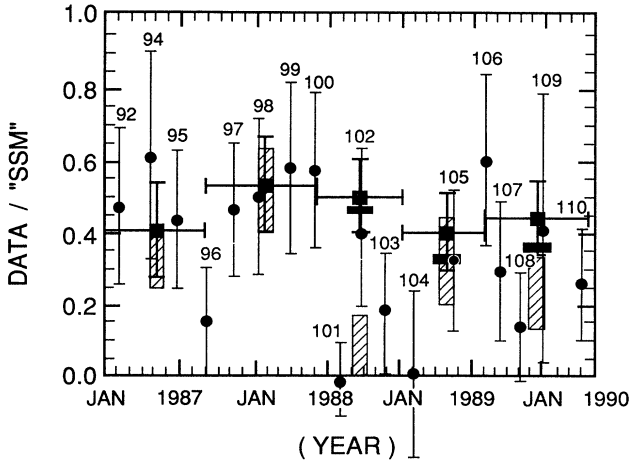

FIG. 34. Comparison of the time variation data of the ^{37}Cl and Kamiokande II detectors during the period January, 1987 through April, 1990, after Ref. [17]. The square points are the Kamiokande II data from Fig. 33(a); the round points are ^{37}Cl data for runs 92–110, except for run 93 which was restricted to a 17-day exposure in the search for neutrinos from SN 1987A. The cross-hatched boxes are the weighted averages of the several ^{37}Cl runs corresponding in time to the time interval of a given Kamiokande II data point. The solid rectangles are the values of the later three Kamiokande II data points from Fig. 33(b).

VII. CONCLUSIONS

The totality of the ^{8}B solar-neutrino data from Kamiokande II provides clear two-part evidence for a neutrino signal from ^{8}B production and decay in the Sun: namely, the directional correlation of the neutrino signal with the Sun, and the consistency of the differential electron energy distribution of the signal in shape and energy scale with that expected from ^{8}B decay. Accordingly, the mechanism of energy generation in the Sun, based on the fusion reactions which give rise to ^{8}B as a by-product, would appear to be unequivocally confirmed by the detection of neutrinos which could only have originated in the core of the Sun.

The measured solar-neutrino flux based on 1040 days of data sample, consisting of subsamples of 450 days (January 1987 through May 1988) at $E_e \geq 9.3$ MeV and 590 days (June 1988 through April 1990) at $E_e \geq 7.5$ MeV, is

$$\text{Data/SSM} = 0.46 \pm 0.05(\text{stat}) \pm 0.06(\text{syst}) \quad \text{(SSM from [7])},$$

and

$$\text{Data / SSM} = 0.70 \pm 0.08(\text{stat}) \pm 0.09(\text{syst}) \quad \text{(SSM from [8])}.$$

During the relatively brief period from January, 1987 through April, 1990, no evidence is present in the Kamiokande II data for a time variation of the ^{8}B solar-neutrino flux.

ACKNOWLEDGMENTS

We gratefully acknowledge the cooperation of the Kamioka Mining and Smelting Company, and the contributions of Katsushi Arisaka and Bruce Cortez to the early stages of this research. This work was supported by the Japanese Ministry of Education, Science and Culture, by the United States Department of Energy, and by the University of Pennsylvania Research Fund. Part of the analysis was carried out by FACOM M780 and M380 at the computer facilities of the Institute for Nuclear Study, University of Tokyo, and part at the Computer Facility of the University of Pennsylvania.

APPENDIX A: DEFINITION OF EFFECTIVE NUMBER OF HIT PMT's

The effective number of hit PMT's (N_{eff}) is defined by

$$N_{\text{eff}} = \frac{948 - N_{\text{dead}}(t_0)}{948 - N_{\text{dead}}(t)} \sum_i \exp\left[\frac{r_i}{l_m}\right] \times \exp\left[-\frac{R}{L_{\text{abs}}}\right] \frac{\cos\theta_i}{f(\theta_i)} \rho_{\text{wall}},$$

where r_i is the distance between PMT$_i$ and the vertex position of an event, l_m is the observed absorption length of the water, θ_i is the angle of the incident light with respect to the PMT$_i$ axis, and $f(\theta_i)$ specifies the acceptance of PMT$_i$. ρ_{wall} is the relative density of PMT's on the particular wall where the PMT is located; $\rho_{\text{wall}}=1$ for the barrel, and $\rho_{\text{wall}}=1.06$ for the top and bottom planes. R (=7.22 m) and L_{abs} (=35m) are constants which indicate the dimension of the detector and an arbitrarily chosen standard of water transparency. The summation is performed for the PMT's with residual time (t_i minus time of flight from vertex to PMT) within ±20 nsec, where t_i is the measured time in PMT$_i$. This time width was determined by the time response of the PMT at the single photoelectron level [13 nsec full width at half maximum (FWHM)]. The first factor in the equation is to correct for the number of dead PMT's $[N_{\text{dead}}(t,t_0)]$, where t and t_0 are the time when the event was detected and a chosen standard time (June 1988).

*Now at NTT, Musashino Research Center, Musashino, Tokyo 180, Japan.
†Now at National Laboratory for High Energy Physics (KEK), Tsukuba, Ibaraki 305, Japan.
‡Now at Institute of Industrial Science, University of Tokyo, Roppongi, Tokyo 106, Japan.
§Now at Maruzen Co., Ltd., Nihonbashi, Tokyo 103, Japan.
**Now at the University of Michigan, Ann Arbor, MI 48109.
†Now at Los Alamos National Laboratory, Los Alamos, NM 87545.

[1] M. Schwarzschild, *Structure and Evolution of the Stars* (Dover, New York, 1965); D. D. Clayton, *Principles of Stellar Evolution and Nucleosynthesis* (University of Chicago Press, Chicago, 1983); J. N. Bahcall, *Neutrino Astrophysics* (Cambridge University Press, Cambridge, England, 1989).

[2] L. Wolfenstein, Phys. Rev. D **17**, 2369 (1978); S. P. Mikheyev and A. Yu. Smirnov, Nuovo Cimento **9C**, 17 (1986); H. A. Bethe, Phys. Rev. Lett. **56**, 1305 (1986).

[3] S. M. Bilenky and B. Pontecorvo, Phys. Rep. **41**, 225 (1978); V. Gribov and B. Pontecorvo, Phys. Lett. **28B**, 493 (1969).

[4] M. B. Voloshin, M. I. Vysotskiĭ, and L. B. Okun, Yad. Fiz. **44**, 677 (1986) [Sov. J. Nucl. Phys. **44**, 440 (1986)]; E. Kh. Akhmedov, Phys. Lett. B **213**, 64 (1988); C.-S. Lim and W. J. Marciano, Phys. Rev. D **37**, 1368 (1988).

[5] For general results and details of the solutions, consult the books in Ref. [1].

[6] R. Davis, Jr., *et al.*, Phys. Rev. Lett. **20**, 1205 (1968); K. Lande *et al.*, in *Proceedings of the 25th International Conference of High Energy Physics,* Singapore, 1990, edited by K. K. Phua and Y. Yamaguchi (World Scientific, Singapore, 1991).

[7] J. N. Bahcall and R. K. Ulrich, Rev. Mod. Phys. **60**, 297 (1988).

[8] S. Turck-Chièze *et al.*, Astrophys. J. **335**, 415 (1988).

[9] This idea has been the subject of a number of papers which are summarized and referenced by Raymond Davis, Jr., Alfred K. Mann, and Lincoln Wolfenstein, Annu. Rev. Nucl. Part. Sci. **39**, 467 (1989), Refs. 66, 72–84.

[10] K. S. Hirata *et al.*, Phys. Rev. Lett. **63**, 16 (1989); **65**, 1297 (1990); **65**, 1301 (1990). See also M. Nakahata, Ph.D. thesis, University of Tokyo Report No. UT-ICEPP 88-01, 1988; S. B. Kim, Ph.D. thesis, University of Pennsylvania Report No. UPR-0174E, 1989.

[11] G. A. Bartholomew *et al.*, Nucl. Data A **3**, 367 (1967).

[12] W. R. Nelson, H. Hirayama, and D. W. O. Rogers, SLAC Report No. 265, 1985 (unpublished).

[13] J. N. Bahcall and B. R. Holstein, Phys. Rev. C **33**, 2121 (1986).

[14] P. O. Lagage, Nature **316**, 420 (1985); L. M. Krauss, S. L. Glashow, and D. N. Schramm, *ibid.* **310**, 191 (1984).

[15] K. S. Hirata *et al.*, Phys. Rev. Lett. **66**, 9 (1991).

[16] K. S. Hirata *et al.*, Phys. Rev. Lett. **61**, 2653 (1988); Astrophys. J. **359**, 574 (1990).

[17] A plot similar to Fig. 34 was shown by R. Davis, Jr., in *Particles and Nuclei,* Proceedings of the Twelfth International Conference, Cambridge, Massachusetts, 1990, edited by J. L. Matthews *et al.* [Nucl. Phys. **A527**, 653C (1991)]. The values for runs 107–110 were provided by R. Davis, Jr., and K. Lande.